

First Extended Catalogue of Galactic Bubbles InfraRed Fluxes from *WISE* and *Herschel** Surveys.

F. Bufano^{1†}, P. Leto¹, D. Carey², G. Umana¹, C. Buemi¹, A. Ingallinera¹,
A. Bulpitt², F. Cavallaro^{1,3,4}, S. Riggi¹, C. Trigilio¹, S. Molinari⁵

¹*INAF-Osservatorio Astrofisico di Catania, Via Santa Sofia 78, I-95123 Catania, Italy*

²*School of Computing, University of Leeds, E C Stoner Building, Leeds, LS2 9JT, UK*

³*Università di Catania, Dipartimento di Fisica e Astronomia, Via Santa Sofia, 64, 95123 Catania, Italy*

⁴*CSIRO Astronomy and Space Science, PO Box 76, Epping, NSW 1710, Australia*

⁵*INAF-Istituto di Astrofisica e Planetologia Spaziale, Via Fosso del Cavaliere 100, I-00133 Roma, Italy*

Accepted ... Received ...; in original form ...

ABSTRACT

This paper presents the first extended catalogue of far infrared fluxes of Galactic bubbles. Fluxes were estimated for 1814 bubbles, defined here as the *golden sample* and were selected from the catalogue produced by Simpson et al. (2012). The golden sample was comprised of bubbles identified within the *WISE* dataset (using 12 μm and 22 μm images) and *Herschel* data (using 70 μm , 160 μm , 250 μm , 350 μm and 500 μm wavelength images). Flux estimation was achieved initially via classical aperture photometry and then by an alternative image analysis algorithm that used active contours. The accuracy of the two methods was tested by comparing the estimated fluxes for a sample of bubbles, made up of 126 H II regions and 43 Planetary Nebulae, which were identified by Anderson et al. (2012). The results of this paper demonstrate that a good agreement between the two was found. This is by far the largest and most homogeneous catalogue of infrared fluxes measured for Galactic bubbles and is a step towards the fully automated analysis of astronomical datasets.

Key words: catalogues; ISM: bubbles; methods: data analysis; techniques: image processing, photometric; infrared: ISM

1 INTRODUCTION

Bubbles are one of the most intriguing objects found within recent large-scale infrared (IR) surveys (see e.g. Churchwell et al. 2006, Mizuno et al. 2010; Wachter et al. 2010; Simpson et al. 2012). The term *bubbles* is used to classify the diffuse emissions with a ring, disc or shell-like shape distributed throughout the entire Galactic plane, although they can be the result of different astrophysical phenomena. For example, some are related to young H II regions, thus to hot massive stars which mold the interstellar medium (ISM), and others to circumstellar envelopes that surround stars at later evolutionary stages, such as Planetary Nebulae (PNe), Luminous Blue Variables (LBVs), Supernova Remnants (SNRs), etc.

Bubble studies enable structural and physical properties

about these objects to be derived. For instance, such work allows important information about their central objects, the stellar winds they arise from and the environment in which they expand to be extracted.

Churchwell et al. (2006; 2007) have catalogued almost 600 bubbles (typically few arcminutes wide), listing the most prominent ones detected in the images from the *Spitzer* Galactic Legacy Infrared Mid-Plane Survey Extraordinaire (GLIMPSE; Benjamin et al. 2003). GLIMPSE surveyed the Galactic plane between sky regions found at $|b| \leq 1 - 2^\circ$ and $|l| \leq 65^\circ$ using four different IR wavebands (3.6, 4.5, 5.8 and 8 μm). Based on the spatial coincidence with known H II regions, Churchwell et al. (2007) claimed that many of the IR bubbles are produced by O and early-B stars. The emission observed with the 8 μm band, in general associated to photo-dissociated regions (PDRs), is mainly due to polycyclic aromatic hydrocarbon (PAH) molecules. These emit via fluorescence at 7.7 μm and 8.6 μm (Tielens 2008), when excited by the far-UV photons from the hot central star. PAH emission at 8 μm from bubbles associated with H II regions is strong, while e.g. in PNe, it

* *Herschel* is an ESA space observatory with science instruments provided by European-led Principal Investigator consortia and with important participation from NASA.

† E-mail: fbufano@oact.inaf.it

is moderately strong or weak/absent if it comes from C-rich or O-rich PNe, respectively (Volk & Kwok 2003; Anderson et al. 2012).

However, analysis of the images from the *Spitzer*/Multiband Imaging Photometer For *Spitzer* Inner Galactic Plane (MIPSGAL, Carey et al. 2009), Deharveng et al. (2010) noticed that the emission at $24\ \mu\text{m}$ of bubbles from Churchwell et al. (2006) is frequently observed inside the bubble with a morphology that closely traces the radio continuum emission at 20 cm from ionized gas. They claimed that the emission at this wavelength is dominated by hot thermal dust, containing a contribution from very small grains (probably silicates) that are out of thermal equilibrium. Mizuno et al. (2010) inspected $24\ \mu\text{m}$ MIPSGAL images, looking for circularly symmetric and extended emissions. They found a total of 416 bubbles, typically smaller than those identified by Churchwell et al. (2006) ($\lesssim 1'$). A fraction of the sample ($\sim 16\%$) was already identified in previous works, and almost the totality of them classified as PNe, LBVs or SNRs, leading the authors to conclude, based also on a strong morphological similarity, that their catalogue included primarily evolved stars.

Nowadays, information from existing IR surveys can help to improve knowledge of the bubble structures and their origins in two ways. Firstly, a larger area of the Milky Way has been covered increasing the number of known objects. Secondly bubbles have been observed in different wavebands. With this purpose, we analyzed: a) the available data from the Wide-field Infrared Survey Explorer (*WISE*), which mapped the entire sky in four IR bands, in particular at $12\ \mu\text{m}$ and $22\ \mu\text{m}$, resembling the $8\ \mu\text{m}$ and $24\ \mu\text{m}$ from *Spitzer* GLIMPSE and MIPSGAL although with a lower resolution; b) the data from the *Herschel* infrared Galactic Plane Survey (Hi-GAL, Molinari et al. 2010), which covers the entire Galactic plane ($|b| \leq 1^\circ$) at longer wavelengths than *WISE* tracing e.g. the distribution of the cold dust (see Section 3).

Despite the richness of information available, only few works exploited such IR data for the bubble studies. Anderson et al. (2012) (hereafter referred to as A12) analyzed a sample of bubbles including 126 H II regions and 43 known PNe with the aim of discriminating between the two kind of sources based on their IR colors. Paladini et al. (2012) published a study on 16 known H II regions in order to understand the mechanisms regulating massive star formation. Both published IR flux catalogues limited to the studied bubbles, where fluxes were estimated by “interactive” methods. Indeed in these analysis, the dimensions of the bubble, thus the radius used for the flux estimation, was visually adjusted and chosen on a case by case basis.

In an era of big data, using only this kind of approach would be simply anachronistic when considering the huge flow of information produced by the incoming unbiased surveys that will be carried out e.g. at the Large Synoptic Survey Telescope (LSST), the James Webb Space Telescope (JWST) or the Square Kilometer Array (SKA).

In this paper, we present two methods for the automated measurement of bubble fluxes and, as final product, a catalogue with the so estimated emitted IR fluxes of a sample of 1814 Galactic bubbles. The paper is organized as follows. In Section 2, we present the selected bubble sample

(whose measured fluxes are published in the final catalogue). In Section 3, we give a description of the technical characteristics of the employed IR surveys and in Section 4 a description of the methods used for the flux measurements is provided. In Section 5, the structure of the published catalogue is presented. Finally, the results are discussed in Section 6 and conclusions given in Section 7.

2 BUBBLE SAMPLE SELECTION

This paper considered the galactic bubble catalogue produced by Simpson et al. (2012) as a database of confirmed bubbles. The catalogue consists of 5106 bubbles that have been identified by citizen scientists via visual inspection of the GLIMPSE and MIPSGAL infrared images, acquired at $8\ \mu\text{m}$ and $24\ \mu\text{m}$, respectively¹. This data set was made by volunteers marking regions of images where bubbles were located. They drew a circular annulus around bubble features and this was scaled in size and stretched into an elliptical annulus resembling the prominent features of bubbles. The identified bubbles have been further split into two groups: 3744 *large*-bubbles, drawn by users as ellipses, and 1362 *small*-bubbles, which were too small to be drawn around in detail but can be still identified. The catalogue lists the centroid position and radius for each bubble, averaged over at least five individual users drawings (see Sect. 3.1 in Simpson et al. 2012 for details). For *large*-bubbles, the catalogue also reports parameters as the inner major and minor axis, outer major diameter, eccentricity and position angle, while the effective radius and thickness values are calculated from geometric means of such diameters (as given in Eq. 1 by Simpson et al. 2012). In particular, since the bubbles were identified on GLIMPSE and MIPSGAL images, they are distributed exclusively over the inner Galactic plane ($|l| \leq 65^\circ$).

As a first step, we selected only those bubbles located in fields observed by the Hi-GAL survey, obtaining a sample of 4988 bubbles over the original 5106, due to the fact that Hi-GAL covers the Galactic latitudes $|b| \leq 1^\circ$ at all Galactic longitudes while *Spitzer* extends at least up to $|b| = 2^\circ$ towards the Galactic center region.

At the same time, we found that a large number of bubbles were projected over each other and therefore could contaminate the final flux estimation. Thus we decided to clean the sample and create a *golden sample*. Firstly we defined a circular region centered on each bubble centroid and with a radius equal to the outer diameter or to the radius given by Simpson et al. (2012) in the case of a *large*- or a *small*-bubble, respectively. Then we selected those bubbles whose circular region is not overlapping with that of any other bubble. We added an extra constraint for the cases where a *small* bubble was overlapping a *large* one. Indeed, having taken for *large*-bubbles the radius equal to the outer diameter in order to guarantee including the totality of the emission at the different wavelength ranges, we risk to remove *small*-bubbles at their very border which are not contaminated. Therefore if the distance between the two centroids was larger than the smallest of the two radii (corresponding in most cases to

¹ <http://www.milkywayproject.org>

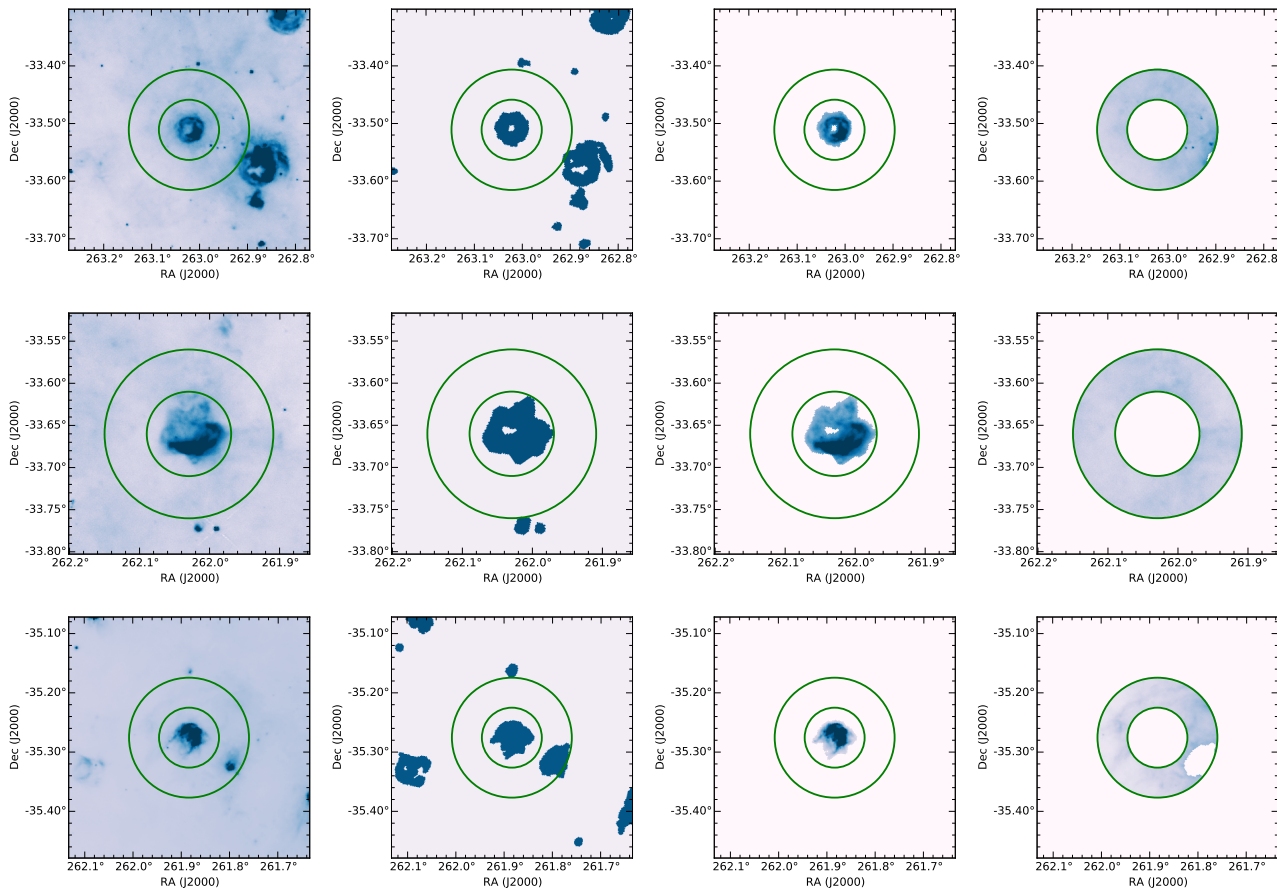


Figure 1. Examples of the application of the two photometric methods on different bubbles, namely 1G354588+000038 (*1st row*), 1G354008+006116 (*2nd row*) and 1G352598-001860 (*3rd row*). *Herschel* images at $70\mu\text{m}$ have been shown for all the images and bubbles aperture and background region of radius R_{ph} and R_{bkg} , respectively, defined with green circles. On the first column, bubbles fields are shown, on the 2nd column the segmentation mask produced for the specific field and in 3rd and 4th column the aperture and background region, respectively, obtained using such mask, as described in Sect. 4.

the *small*-bubble radius) then both bubbles were kept separated and included in the golden sample. In addition this enabled duplications of single bubbles present in both catalogues to be removed. The selected final sample consisted of a total of 1814 bubbles: 45% of the *small*-bubbles from Simpson et al. (2012) were kept, whilst 33% of the *large*-bubbles. Nonetheless, the *large*-bubbles still represent two thirds of the golden sample. A catalogue for this has been produced, listing for each bubble the relative Galactic coordinates (corresponding to their centroids) and their radius (R_{cat}), which is either equal to the bubbles effective radius or to half of its outer diameter for the case of *small*- and *large*-bubbles respectively.

3 DATA DESCRIPTION

The images from which we estimated the fluxes emitted by the bubbles of the golden sample are taken from the *WISE* and Hi-GAL surveys.

3.1 *WISE* image database

WISE (Wright et al. 2010) was a mission that mapped the entire sky in four IR bands, namely $3.4\mu\text{m}$, $4.6\mu\text{m}$, $12\mu\text{m}$ and $22\mu\text{m}$ (data used here was from the March 14, 2012 release).

In this work we used the $12\mu\text{m}$ and $22\mu\text{m}$ bands, since they trace similar dust components as that of GLIMPSE $8\mu\text{m}$ and MIPS GAL $24\mu\text{m}$ bands, respectively. However, the $12\mu\text{m}$ bandpass is significantly broader than GLIMPSE’s $8.0\mu\text{m}$, collecting emissions from PAH features at $11.2\mu\text{m}$, $12.7\mu\text{m}$ and $16.4\mu\text{m}$ (Tielens 2008). The PAH features at $7.7\mu\text{m}$ and $8.6\mu\text{m}$ also fall within the bandpass although at diminished sensitivity. The spatial resolutions in the two bands are $6''.5$, and $12''$ and the sensitivities are 1 mJy and 6 mJy , respectively. The *WISE* image data have units of DN, thus we used a DN- to-Jy conversion factor equal to 1.8326×10^{-6} and 5.2269×10^{-5} for the $12\mu\text{m}$ and $22\mu\text{m}$ bands, respectively (see *WISE* explanatory supplement²).

² http://wise2.ipac.caltech.edu/docs/release/allsky/expsup/sec2_3f.html

3.2 *Herschel* image database

The Hi-GAL survey was performed using the Photoconductor Array Camera and Spectrometer (PACS; Poglitsch et al. 2010) and the Spectral and Photometric Imaging Receiver (SPIRE; Griffin et al. 2010) instruments onboard the *Herschel* Space Observatory (Pilbratt et al. 2010). Hi-GAL maps the Galactic plane ($0^\circ \leq l \leq 360^\circ$, $|b| \leq 1^\circ$) in five wavebands, namely $70\ \mu\text{m}$, $160\ \mu\text{m}$, $250\ \mu\text{m}$, $350\ \mu\text{m}$ and $500\ \mu\text{m}$, providing a well-sampled coverage of the frequency range where the spectral energy distribution of cold dust peaks. The spatial resolutions of these images are $6''.7$, $11''$, $18''$, $25''$, and $37''$, respectively. Images were reduced using the ROMAGAL data-processing code, for both PACS and SPIRE data (see Traficante et al. 2011 and Molinari et al. 2016 for details).

4 BUBBLE FLUX MEASUREMENTS

We estimated the flux coming from each of the 1814 bubbles belonging to the golden sample using two different methods: the first method is a classical aperture photometry, in which we measured the flux within a circular area centered on the source; the second one uses the same aperture but selects the flux coming from the bubble using a segmentation mask, which removes any pixel coming from nearby contaminating sources and from the background. Before applying such methods, we prepared our sample images, as described in the following subsection.

4.1 Dataset Preparation

Using the selected golden sample catalogue, sources were cut out of the *WISE* and *Herschel* image datasets using a bounding box that was centered on the bubbles centroid and whose width was equal to 10 times R_{cat} . Each map (cut out) was projected onto the N-E equatorial direction and scaled to the pixel scale of a reference image using the Montage toolkit³. The image taken as reference was the one with the smallest pixel scale, i.e. the *WISE* image at $12\ \mu\text{m}$ ($1.37''/\text{pix}$). This allowed seven images to be produced for each source with an identical pixel grid.

4.2 Photometric Methods

4.2.1 Aperture Photometry

We estimated the flux coming from each source in different bands measuring the flux falling into a circular area centred on the bubble centroid coordinates given by Simpson et al. (2012), with a radius (R_{ph}) chosen equal to

$$R_{ph} = \sqrt{(2R_{cat})^2 + (FWHM)^2} \quad (1)$$

where FWHM is the beam size for each bandpass, in order to include all the flux coming from the bubble in different bands. The local background level has been estimated just outside the aperture, over an annular area between R_{ph} and $2R_{ph}$ and is equal to the sigma-clipped mean ($2\text{-}\sigma$ level). This was chosen to remove very bright compact objects or

spurious spikes. The average background level has then been subtracted from each pixel value within the source aperture, before computing the total aperture flux of the bubble.

Segmentation Photometry – This method made use of a “segmentation mask” to select the flux coming from each bubble. In image processing, segmentation is the process of partitioning of a digital image into its component parts and that was used here to define bubble regions. To enable the segmentation of bubbles, a localised *active contours* algorithm (Lankton & Tannenbaum 2009) was used that also incorporated gradient information via *Magnetostatic forces* (Xie & Mirmehdi 2008). In our paper’s approach, many of the difficulties associated with the use of localised contours were overcome by adaptively selecting the appropriate kernel sizes that are required by this algorithm (further details in Appendix A). In other words, this paper’s active contour algorithm finds bright objects that have large gradients. In images where there are many high gradient regions, the contour could grow wildly around the image, at least without human intervention, which is not feasible in this case. This was the case for *Herschel* images acquired at $\geq 160\ \mu\text{m}$ as they had high background contamination. The same is true for *WISE* images at $12\ \mu\text{m}$ as they contained numerous compact field objects. Thus we decided to optimize the method on the $70\ \mu\text{m}$ images, since bubble contours at this band generally include those at shorter wavelengths and, at the same time, trace dust distribution better than longer ones.

Thus segmentation masks have been obtained from original *Herschel* $70\ \mu\text{m}$ images, and consequently they have the same pixel scale. Since bubbles images were resampled to the *WISE* $12\ \mu\text{m}$ pixel scale (as described in section 4.1), we also performed the resampling of the segmentation mask to make them match. Moreover, in order to take into account the instrumental effect on the bubbles contours in images at lower resolution than $70\ \mu\text{m}$ images, we convolved the mask with a Gaussian profile to correct the beam size differences, before applying it to the corresponding image. This smoothed the mask borders and mimicked the instrumental effect, assigning a fractional value between 0 and 1 to each pixel, which was finally replaced with 1, to produce the new mask.

By using the segmentation map, we mask anything falling in the aperture R_{ph} but not expected to be part of the bubble. Any other bright segmented source falling in the background annulus was also removed, before estimating the average background level value. As a consequence a shallower clipping level ($3\text{-}\sigma$) than in the aperture method was used. The average background level has been subtracted from each pixel value in the aperture region masked as the bubble, and then summed to estimate the flux of the bubble (“segmentation” flux). Comparing the background average level estimated in this way with that of the aperture photometry, we found that they are in agreement within 5% for 85% of the bubbles. Aperture background level turned out to be higher than the segmentation one in around 8% of the cases, most frequently when the presence of extended emission in the background region increased the background sigma value and thus made the sigma-clipping less effective. In other cases (around 7%), the segmentation did not work correctly in masking bright nearby sources,

³ <http://montage.ipac.caltech.edu/>

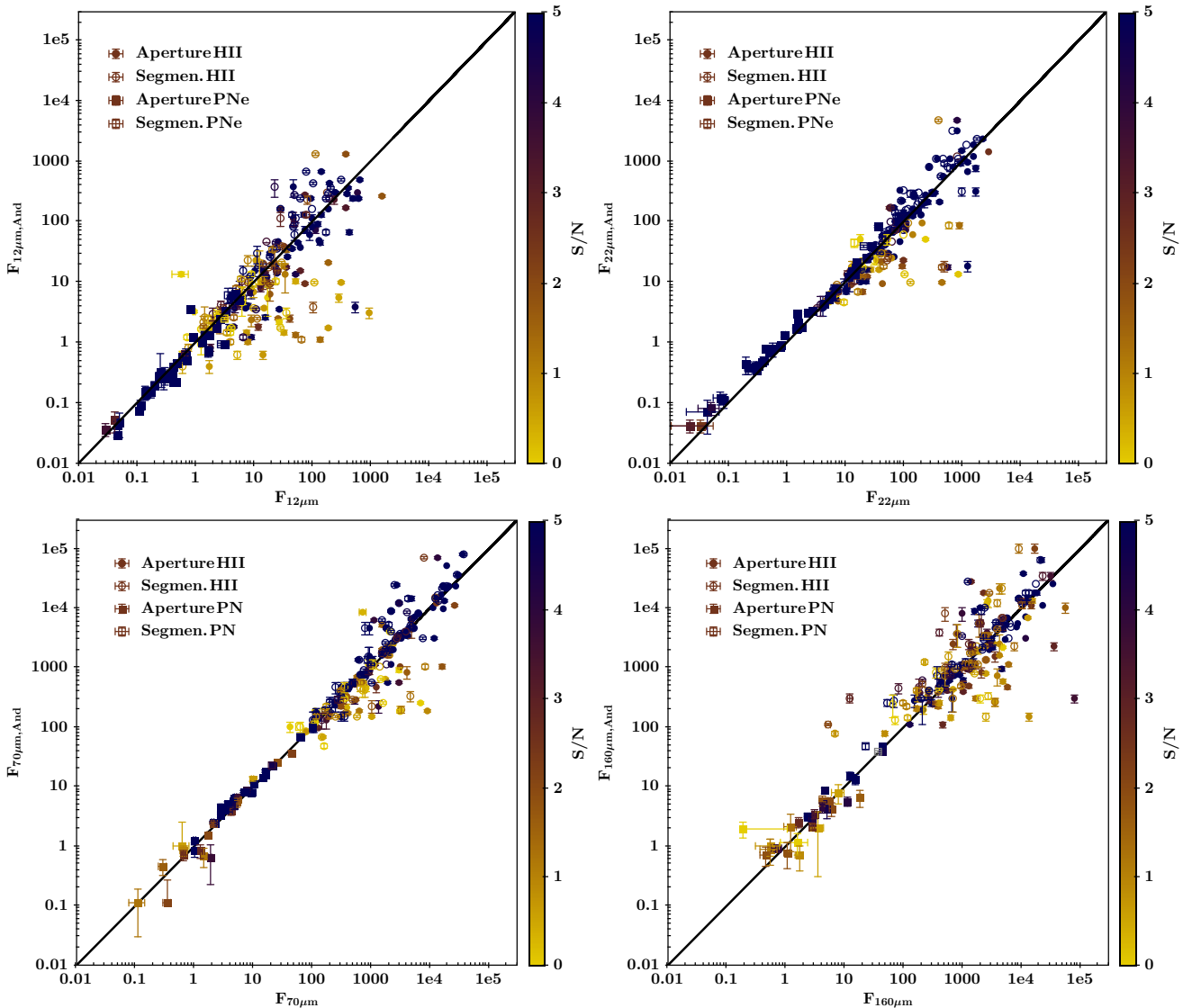


Figure 2. Comparison between photometry obtained with our automated methods and A12 results. Fluxes from H II regions are reported with circles and PNe with squares. For aperture photometry filled dots are used, while dots for the segmentation photometry are empty. Fluxes are given in Jy. The color scale indicates the S/N characteristic of each of our measurements.

causing a higher average background level.

Examples of the application of the two photometric methods are shown in Figure 1. We did not provide flux measurements at a given wavelength for those bubbles that exceed 10% of saturated pixels within R_{ph} , since with such high fraction of 'NaN' values the bubble flux estimate would not be reliable. In any case, they represent a very small fraction of the total sample (24/1814 for *WISE* images and 4/1814 within *Herschel* images acquired at 250 μm and 500 μm and 2/1814 for *Herschel* images taken at 350 μm).

For both methods, the uncertainty on the flux is calculated as the sum in quadrature of the background and source counts error over the total number (N) of pixels within R_{ph} over which the flux was calculated. Source counts error is equal to the photon noise in the case of *WISE* images, or to the calibration uncertainties for the *Herschel* maps due

to the uncertainties in the theoretical models of the SED of the calibrators and equal to 5% of the flux for PACS images (Balog et al. 2014) and to 4% for those from SPIRE (Bendo et al. 2013). Background error is given by the sum in quadrature of the photon noise/calibration error within the background annulus and the background standard deviation.

Additionally, along with the measured total flux and the relative uncertainty, we provide a value, reported as S/N, which corresponds to the ratio between the median of the background subtracted pixel values within R_{ph} and the background standard deviation. Such values can be used as an indicator of the significance of the detection with respect to the background level.

Finally, we assumed that the contamination from bright compact sources falling in the aperture is negligible, based on the results of previous work, i.e. A12, and of a statistical analysis conducted on this paper data. A12 found that

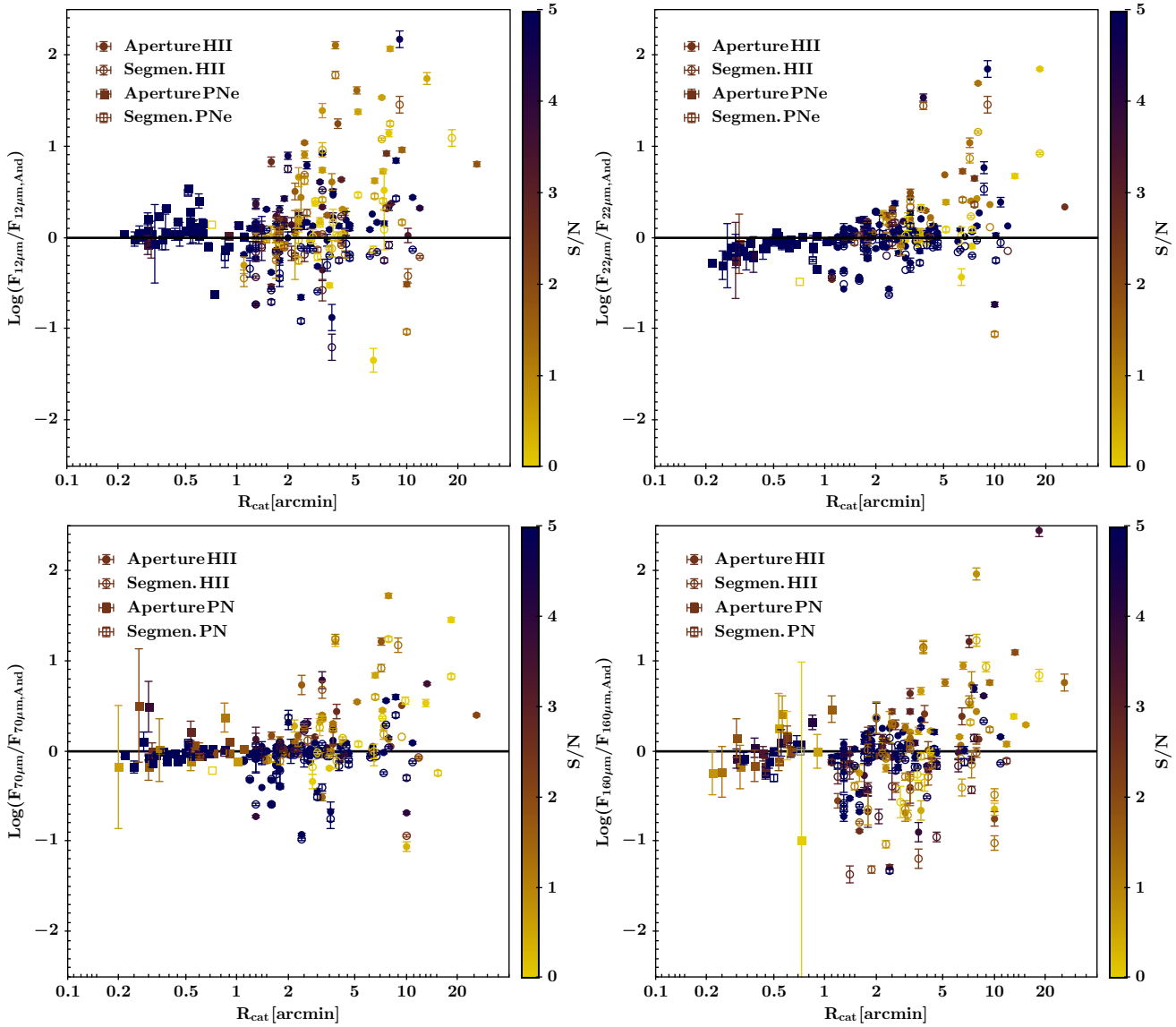


Figure 3. Distribution of flux differences between our methods and A12 measurements as function of the angular extension of the bubble. Fluxes from H II regions are reported with circles and PNe with squares. For aperture photometry filled dots are used, while dots for the segmentation photometry are empty. Radii are given in arcminutes. The color scale indicates the S/N characteristic of each of our measurements.

as H II regions are in general much brighter than any point source within the aperture, the removal of such point sources has a minimal impact on the derived fluxes. In the same way, for less extended bubbles, such as PNe, the small characteristic angular size makes it unlikely that there is a spatial coincidence with point sources. Therefore, there is likely to be no consequent contamination of the bubble flux. Possible contribution by compact objects to the bubbles flux measured in this paper was also checked. Assuming that compact objects are mainly stars, we estimated their flux contribution at $12\mu\text{m}$, considering that stellar spectral energy distribution is usually the strongest at this wavelength, relative to others used in this paper. From the AllWISE

Source Catalogue⁴, we selected the compact objects consistent with a single Point Spread Function and with no saturated pixels, located in the same sky region of the golden sample bubbles. We cross-matched the two catalogues and found the number of compact objects included in the aperture radius of each bubble, calculating their total flux and contribution to the bubble aperture flux. We found that for *large*-bubbles the fraction of bubbles with a flux contamination higher than 10% is around 25% (298/1181), while for *small*-bubbles such fraction is around 15%. This confirms the marginal contribution of compact objects to the bubbles measured flux already at $12\mu\text{m}$, which is expected to be the most affected band by the contaminants. It is worth

⁴ <http://irsa.ipac.caltech.edu/cgi-bin/Gator/nph-scan?submit=Select&projshort=WISE>

to stress that 3% of the *small*-bubbles has a contamination higher than 50% most likely due to the coincidence of the compact object with the bubble itself. Most importantly, no compact objects are included in the aperture radii of one third of the *small*-bubbles.

4.3 Comparison with Anderson et al. (2012)

Recently, A12 analyzed the distribution of FIR emissions from H II regions and PNe in order to find a criterion to discriminate between these objects simply using their IR colours. They collected a sample of 43 PNe and 126 H II regions. In order to test their diagnostic method, H II regions have been carefully chosen to span a wide range of angular sizes ($1'.1 \leq R \leq 25'.9$). In particular, they pay attention at including small size H II regions, i.e. young compact H II regions in early evolutionary stages or more evolved H II regions at extreme distances from the observer, since they can be easily mistaken with typical PNe, having similar dimensions. The sample of objects presented, both H II regions and PNe, is numerically limited but it is composed of bright examples of these classes, thus they are relatively unconfused with nearby sources of emission. A12 provided the fluxes of these (126+43) bubbles at different IR bandpasses, including 12 μm and 22 μm from *WISE* and 70 μm , 160 μm , 250 μm , 350 μm and 500 μm from *Herschel*.

We decided to apply our automated methods to the same object sample and compare our estimated fluxes with those measured by A12, as a quality check of our results. They measured the fluxes emitted by the H II regions within an aperture of arbitrary size fixed manually and shaped in a way that includes all the associated emission at all wavelengths and excludes contaminating compact bright sources in the field. The assumption of a unique aperture is considered conservative and safe by the authors, since most of their H II regions are bright at IR wavelengths and have a similar morphology and angular extension at all wavelengths, but implies some form of human intervention for deciding the shape. On the other hand, considering the small angular size of PNe, their photometry is more sensitive to the choice of a unique aperture size for all the wavelengths, thus they chose to adopt individual apertures at each bandpass. A12 published the measured fluxes along with the aperture radius used for each H II region and that at 24 μm for PNe. Using radii from A12 catalogue as the dimension (R_{cat}) of the bubbles and applying, as previously described, the two methods, we obtained for each bubble the aperture and segmentation fluxes. The comparison between our flux estimates and those from A12 have been plotted in Figure 2: aperture photometry for the H II regions (circles) and PNe (squares) is reported using filled dots, while the empty ones refer to the segmentation photometry. First in Figure 2, we reported the comparison at 12 μm , 22 μm , 70 μm and 160 μm , since at these wavelengths the bubble is brighter and the estimate less sensitive to the background variation, as discussed later in this section. A general agreement is visible among the flux measurements, especially for the PNe, while a larger scatter is present for the H II regions. The latter could be explained with a stronger contamination by the background to the more extended bubbles. This is more evident in Figure 3, in which flux ratios, expressed as

$$\Delta Log = Log F_{\lambda} - Log F_{\lambda,And} = Log(F_{\lambda}/F_{\lambda,And}) \quad (2)$$

are plotted as function of bubble angular extension. We also note that among extended bubbles, those with a large difference in flux with respect to A12 have also a very low S/N. At the same time, we found from a visual inspection of the few bubbles with a large scatter but high S/N (affecting in particular the H II regions), that the R_{cat} value reported by A12 could largely under- or over-estimate the real dimension of the bubble.

For this reason, in order to estimate an average $\langle Log(F_{\lambda}/F_{\lambda,And}) \rangle$, that could express the reliability of our methods, we removed values which differ more than $2\text{-}\sigma$ from the mean. Average $\langle \Delta Log \rangle$ are reported for each bandpass in Table 1. For the aperture photometry, we also provided the total number of bubbles from A12 sample detected in our images, as well as the number of *bright* bubbles. We labelled bubbles with positive flux as *bright*, in contrast with those sources, which are faint over a possibly complex background and have been consequently discarded. In a similar way, for segmentation photometry we reported the total number of detected bubbles successfully masked (*segmented*) and the corresponding number of bright bubbles. Finally, for both methods we gave the sample of bright bubbles used to compute the average after the $2\text{-}\sigma$ clipping (*clipped* bubbles). Similarly for A12 sample, we indicated the number of bright bubbles, i.e. bubbles with a no-null flux measurement by A12, over the total one. Results for bandpasses at $\lambda \geq 250 \mu\text{m}$ are shown in Figure 4.

In Figure 5, we reported the histograms of ΔLog for each bandpass: histograms are shown for both methods and refer to the distribution of the bright bubbles sample and of the more limited one, selected after the clipping (*clipped sample*). From Figure 5, we can notice that there is in general a very good agreement between the two flux estimates. In particular, the difference between our aperture photometry and A12, is less than 5% at 22 μm , 70 μm and 160 μm , and increases to about $\sim 25\%$ at longer wavelengths, where we expect the emission from the bubble to be less intense relative to the background. The $\langle \Delta Log \rangle$ at 12 μm is also $\sim 28\%$, even though we used the old DN-to-Jy conversion factor (2.9045×10^{-6} from the Explanatory Supplement of the Preliminary data release products), as A12 did, to make results consistent.

Moving to the comparison with the results obtained with the segmentation method, we found that the segmentation method has a good agreement at shorter wavelengths ($\langle (1 - F_{\lambda}/F_{\lambda,And}) \rangle < 10\%$), and a larger difference ($\sim 25\text{-}35\%$) at longer ones. In particular, we can notice that it tends to provide on average lower fluxes ($\langle \Delta Log \rangle < 0$): this is likely due to the fact that the segmentation helps in better masking the flux falling in the aperture, allowing only that coming from the sources to be selected and removing the contaminating flux from the background. The origin of such differences could also be in the method, which could generally be too strong and likely remove the pixels of the more external parts of the bubble. On the other hand, as already discussed in Sect. 4.2, in this work we chose to obtain the masks from 70 μm images, knowing that 70 μm emission contours generally include those at shorter wavelengths. Moreover, we can assume that bubble shape at $\lambda > 70 \mu\text{m}$ does not change significantly, since emissions at such wavelengths originate

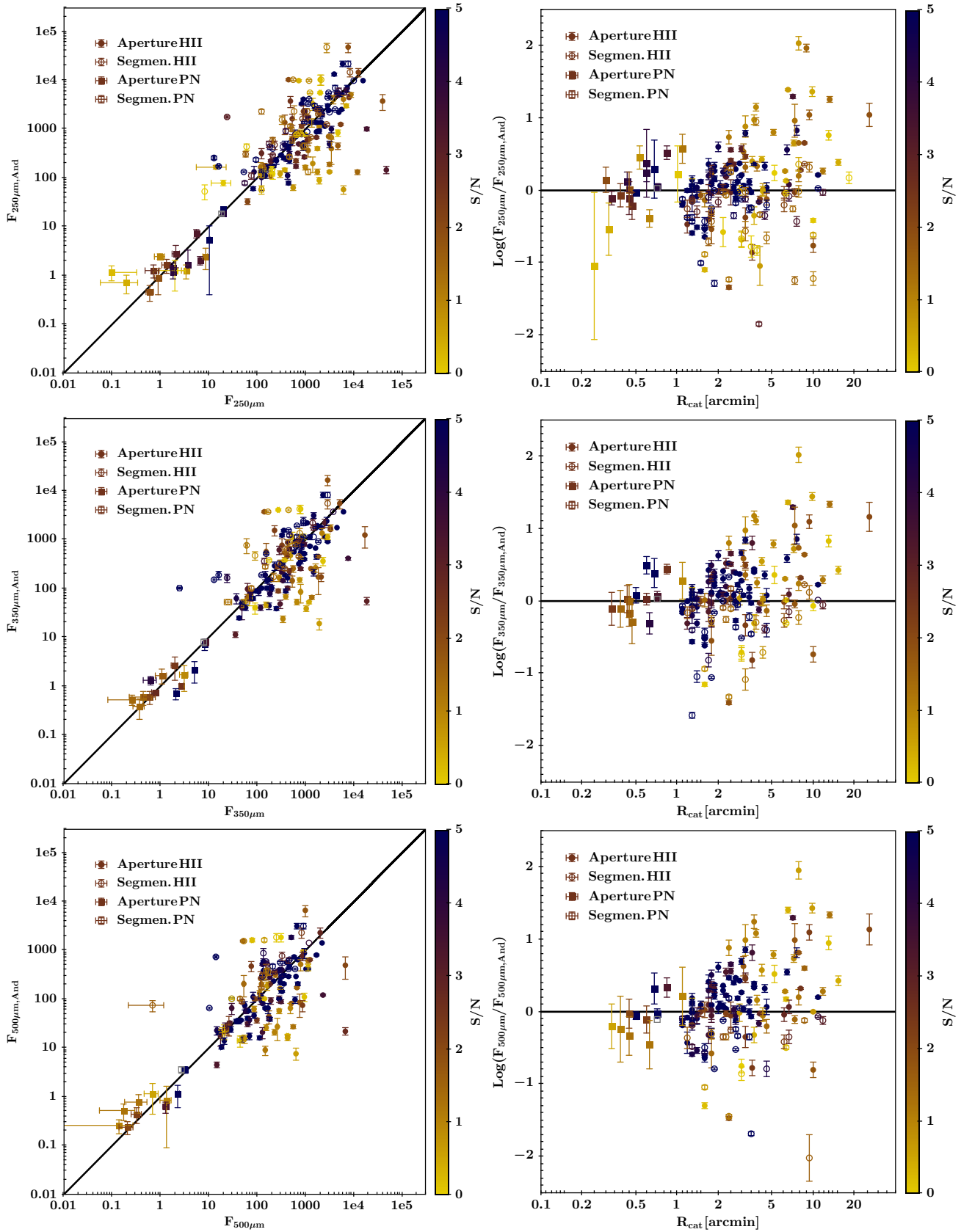


Figure 4. *Left Column:* Comparison between photometry obtained with our automated methods and A12 results at 250 μm , 350 μm and 500 μm . Fluxes from H II regions are reported with circles and PNe with squares. For aperture photometry filled dots are used, while dots for the segmentation photometry are empty. Fluxes are given in Jy. *Right Column:* Distribution of flux differences between our methods and A12 measurements as function of the angular extension of the bubble. Radii are given in arcminutes. In all the plots, the color scale indicates the S/N characteristic of each of our measurements.

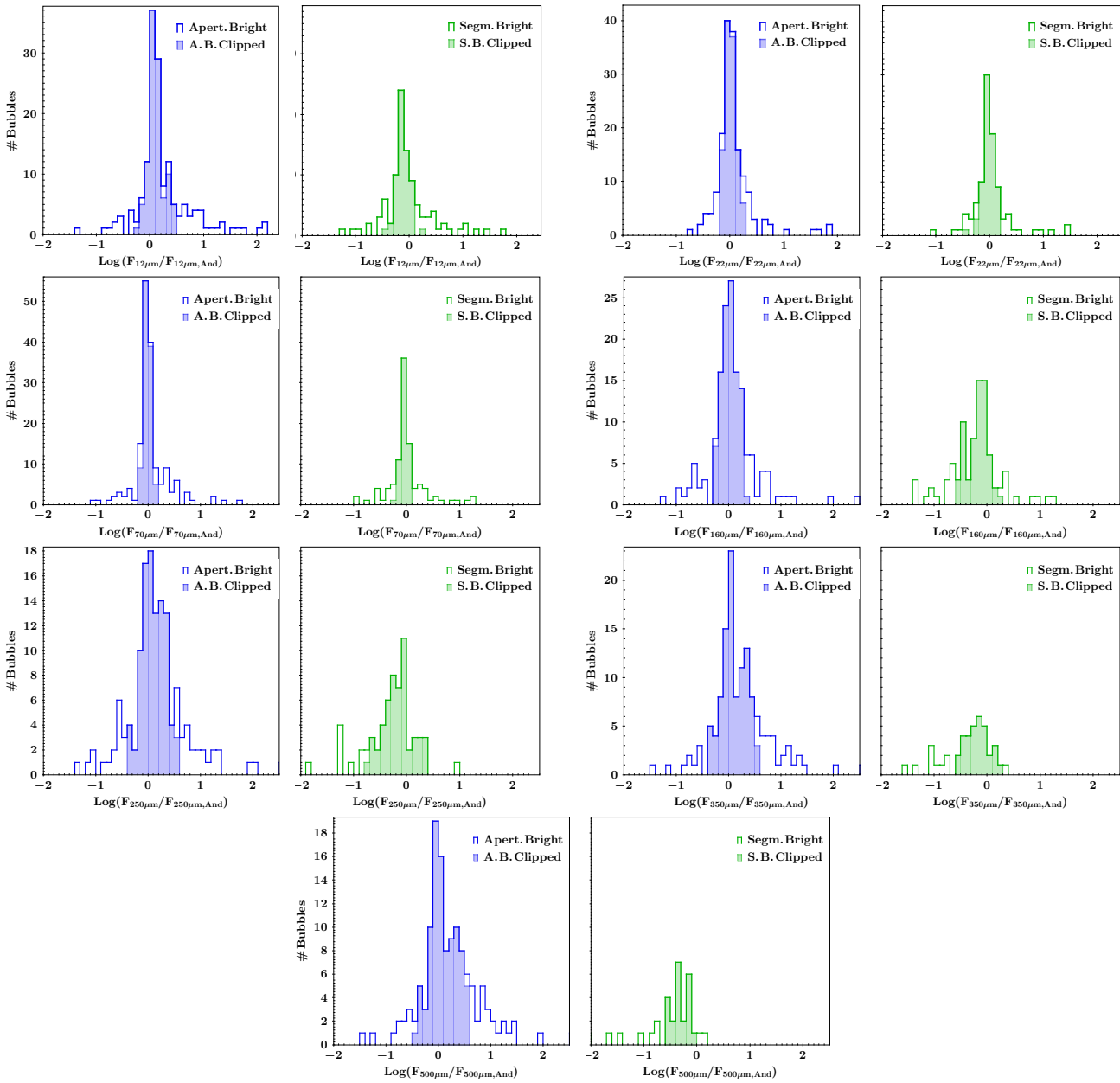


Figure 5. Histograms of the distribution of the difference ΔLog between fluxes from this work and A12. For each photometric method, bubbles samples (H II regions plus PNe) are formed by the total bright bubbles sample or by the limited one (“clipped”), selected after the sigma-clipping (2σ level). These are reported with empty and filled histograms respectively.

from the same component of the bubble, namely the cold dust. As a consequence, the estimated discrepancies (ΔLog) can be more likely arisen from background contamination, which largely increases at redder bandpasses.

Finally, it is worth noticing that, when we considered the results on PNe of the segmentation method, we found that the active contours failed in finding most of the bubbles, possibly because of their small angular size and/or of a possible faint emission of such objects at $70\ \mu\text{m}$. We discuss about the reason of the segmentation method failure in finding bubbles contours in Section 6.

5 CATALOGUE FORMAT

As an example of the final catalogue, we reported in Appendix B tables with the fluxes measured with the two methods for a collection of bubbles taken from the golden sample: *WISE* $12\ \mu\text{m}$ and $22\ \mu\text{m}$ values are given in Table B1 and Table B2, respectively and *Herschel* $70\ \mu\text{m}$, $160\ \mu\text{m}$, $250\ \mu\text{m}$, $350\ \mu\text{m}$ and $500\ \mu\text{m}$ values in Table B3 and Table B4.

All the Tables give the source name followed by the Galactic longitude and latitude and the angular size (R_{cat}) taken from Simpson et al. (2012) and used, as previously described (Sect. 2), in our work. Total flux (F_λ) is given in Jy, as well as the associated uncertainty.

Table 1. Average difference between fluxes from this work and A12, where ΔLog has been calculated as in Eq. 2. The number of bubbles composing the “detected”, “bright” and “clipped” sample (see Sect. 4.3) are given

Aperture Photometry					
Band	$\langle\Delta\text{Log}\rangle$	H II region		PN	
		Clip./Bright/Detect.	Bright/Detect.(A12)	Clip./Bright/Detect.	Bright/Detect.(A12)
12 μm^a	0.11 ± 0.14	73/115/126	126/126	32/39/43	40/43
22 μm	0.01 ± 0.10	84/123/126	126/126	31/41/43	42/43
70 μm	-0.01 ± 0.06	75/122/126	126/126	33/43/43	43/43
160 μm	0.02 ± 0.14	81/120/126	126/126	24/28/43	31/43
250 μm	0.10 ± 0.20	81/121/124	126/126	17/19/43	21/43
350 μm	0.10 ± 0.22	84/120/126	126/126	14/14/43	16/43
500 μm	0.09 ± 0.23	83/120/126	126/126	11/11/43	12/43
Segmentation Photometry					
Band	$\langle\Delta\text{Log}\rangle$	H II region		PN	
		Clip./Bright/Segmen.	Bright/Detect.(A12)	Clip./Bright/Segmen.	Bright/Detect.(A12)
12 μm^a	-0.12 ± 0.11	57/94/94	126/126	4/4/4	40/43
22 μm	-0.02 ± 0.11	68/94/94	126/126	4/4/4	42/43
70 μm	-0.04 ± 0.07	59/97/97	126/126	4/4/4	43/43
160 μm	-0.18 ± 0.18	61/86/95	126/126	2/2/4	31/43
250 μm	-0.16 ± 0.26	52/62/98	126/126	1/1/4	21/43
350 μm	-0.18 ± 0.20	31/41/97	126/126	1/1/4	16/43
500 μm	-0.31 ± 0.15	21/30/98	126/126	1/1/4	12/43

^a Similarly to A12, for *WISE* 12 μm it has been used a different DN-to-Jy conversion factor, equal to 2.9045×10^{-6} taken from the Explanatory Supplement of the preliminary data release products.

Missing flux estimates are indicated with a “-” if the survey image only partially covers the bubble or in case it has a high fraction of saturated/NaN pixels ($>10\%$), since in both cases the measurement would not be reliable. In the *WISE* images, there are 24 missing bubbles, all of them discarded for a high fraction of saturated pixels, while for *Herschel* there are a maximum of 7 (for 250 μm and 500 μm images) with about half of them not completely covered. The number of the remaining bubbles, with “positive” detection is reported in Table 2 (*Detected* bubbles) for each bandpass together with their percentage with respect to the whole golden sample catalogue (1814 bubbles).

Flux estimates are indicated with a “***” when the emission of the bubble is too faint, i.e. the source average flux per pixel is lower than the estimated average background level. Thus in Table 2, we reported also the total number of *bright* bubbles (all the bubbles with a flux estimate listed in the catalogue) and their percentage with respect to the number of detected bubbles. In the case of the segmentation photometry, a measurement of the flux could also be missing (indicated with a “-”) when the active contours method fails in finding the bubble, i.e. no segmentation mask corresponding to the bubble is produced. Also in this case we report the number of *segmented* bubbles with the relative fraction over the detected sample, and the number of *bright* bubbles along with the fraction respect the segmented one. Table 2 thus gives a global view of what is available in the entire flux catalogue.

6 DISCUSSION

Fluxes obtained from the aperture and segmentation method are presented in Figure 6. For each bubble, we plotted the aperture photometry flux against the segmentation one, with the size of the dots proportional to the logarithm of the bubbles radius (R_{cat}) and the color scaled based on the S/N of the corresponding aperture flux estimation. The latter efficiently conveys the brightness of a source over the possible complex background. We defined the ratio between the two flux measurements for each bubble as

$$\Delta M_\lambda = \text{Log}F_{\lambda,Ap.} - \text{Log}F_{\lambda,Segm.} = \text{Log}(F_{\lambda,Ap.}/F_{\lambda,Segm.}) \quad (3)$$

and plotted it as a function of the angular dimension of the bubble in Figure 7. In Table 3, we reported the average $\langle\Delta M_\lambda\rangle$ value for each bandpass, obtained after clipping values more than $3\text{-}\sigma$ away from the average. The total numbers of detected/clipped bubbles sample are also given. A very good agreement between aperture and segmentation photometry is visible at 70 μm , where $\langle F_{\lambda,Ap.}/F_{\lambda,Segm.}\rangle$ is close to 1, giving a relative difference of around 7%: this bandpass is the one that better quantifies the deviation between the two methods, since the segmentation masks are produced using the images taken at this wavelength, thus the contours best trace the bubble shape. Consequently, we can assess that at 70 μm the aperture photometry fluxes are generally slightly larger than the segmentation ones. This is what we found also in the comparison of the two methods at the other bandpasses, having convolved the mask to reproduce instrumental differences from 70 μm images, but also assumed a physical similar shape. Higher aperture flux is likely ascribable to the contamination in

Table 2. Bubbles sample listed in the IR flux catalogue.

Bandpass	Aperture Photometry				Segmentation Photometry			
	Detected	% ^a	Bright	% ^b	Segmented	% ^c	Bright	% ^d
12 μm	1790	98.6%	1704	95.2%	1018	56.9%	1014	99.6%
22 μm	1791	98.7%	1726	96.4%	1019	56.9%	1017	99.8%
70 μm	1814	100.0%	1763	97.2%	1024	56.5%	1024	100.0%
160 μm	1814	100.0%	1763	97.2%	1024	56.4%	663	64.7%
250 μm	1807	99.6%	1675	92.7%	1022	56.6%	351	34.3%
350 μm	1811	99.8%	1655	91.4%	1022	56.4%	208	20.3%
500 μm	1807	99.6%	1635	90.5%	1022	56.6%	143	14.0%

^a Percentage of Detected bubbles over the 1814 from the golden sample.

^b Percentage of Bright bubbles over the Detected ones

^c Percentage of Segmented bubbles over the Detected ones.

^d Percentage of Bright bubbles over the Segmented ones

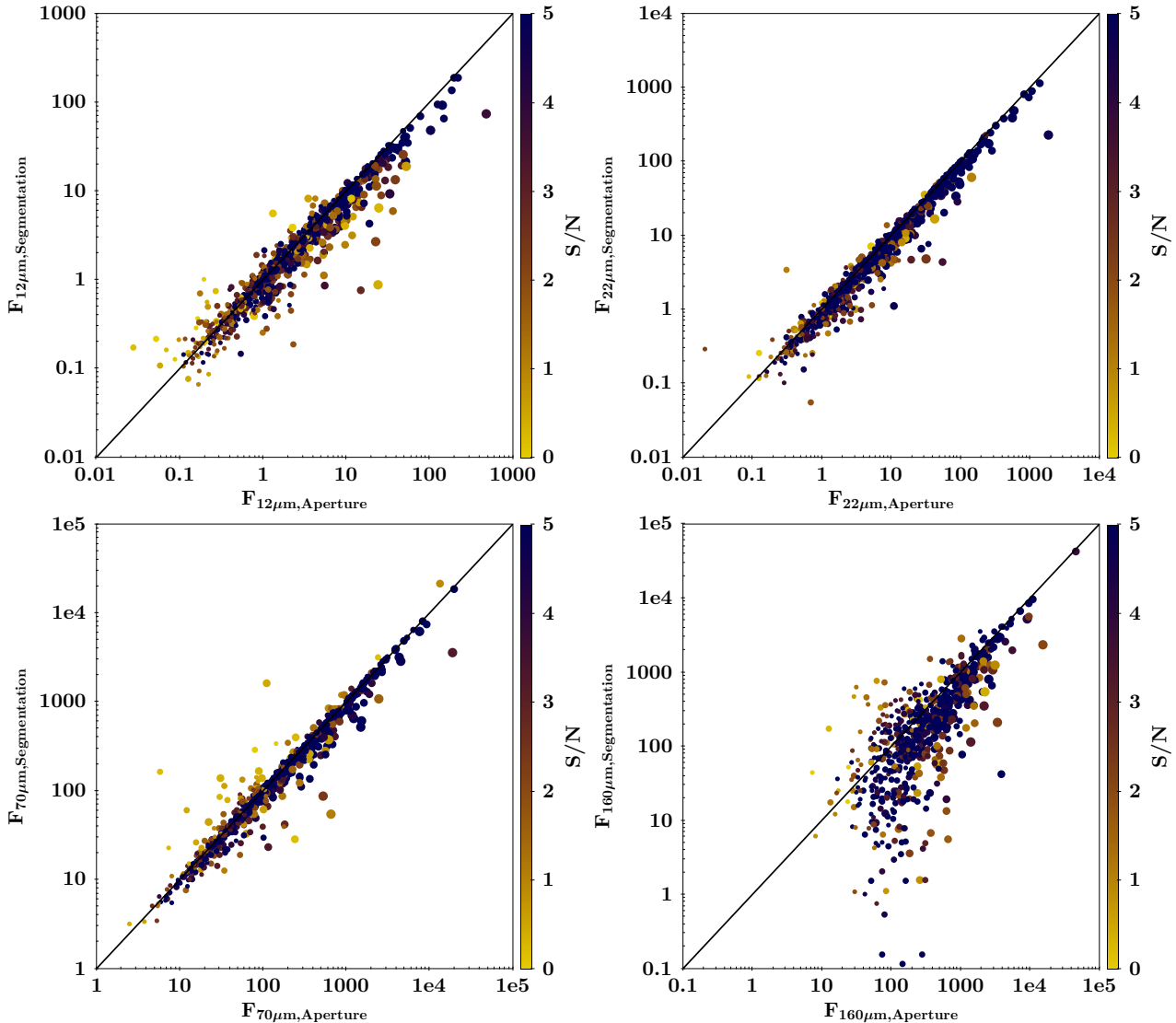


Figure 6. Comparison of flux estimates using the aperture photometry against the segmentation one. Dots size is proportional to the logarithm of the bubble radius (R_{cat}) and the color scales based on the S/N of the relative aperture flux estimation.

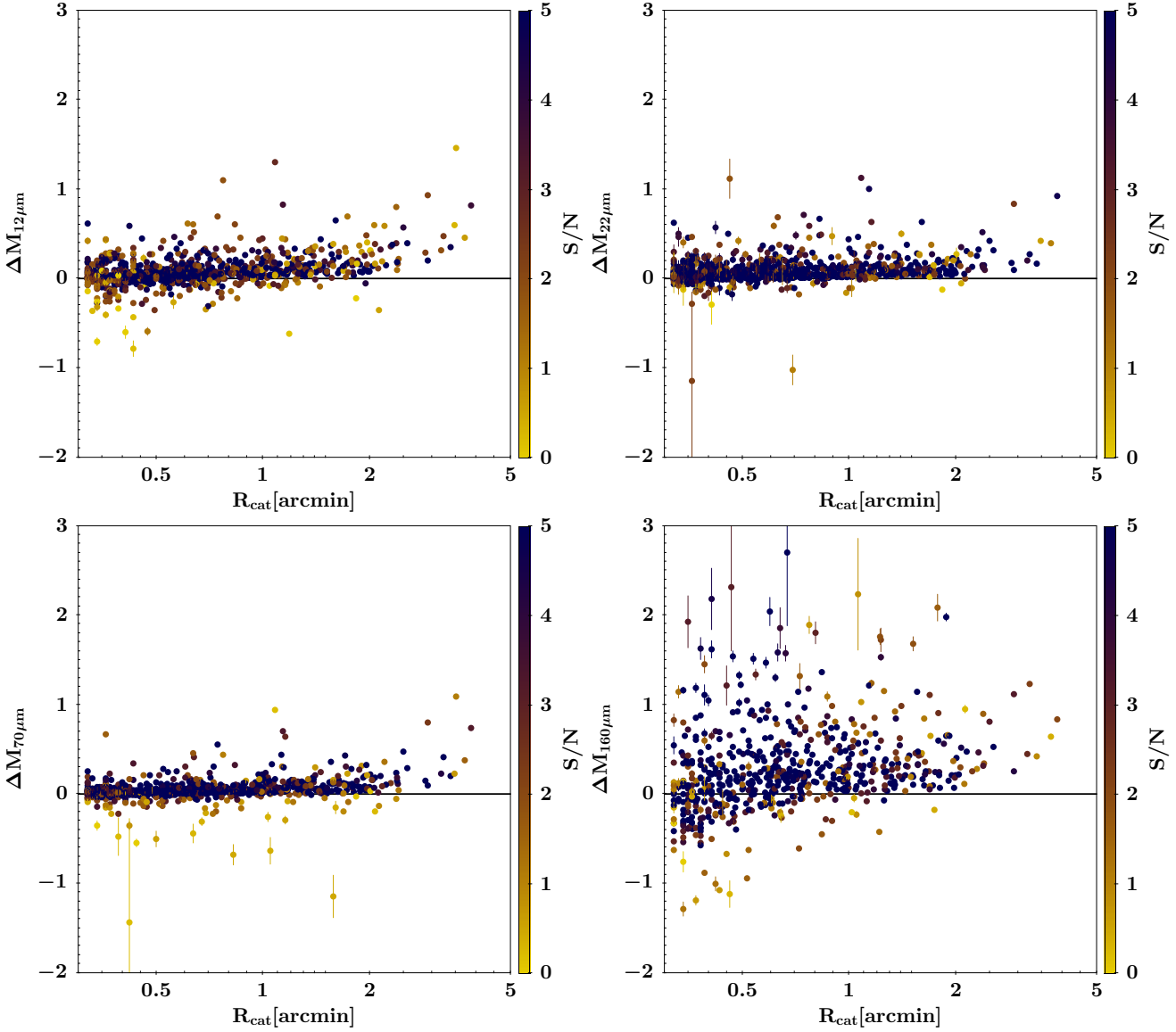


Figure 7. Distribution of flux differences between aperture and segmentation photometric method as function of the angular extension of the bubble. Radii are given in arcminutes. The color scales based on the S/N of the relative aperture flux estimation.

the aperture method from the local background flux that cannot be totally removed by subtracting the average level and/or that falls within the aperture but “outside” the bubble contours as defined by the segmentation method. The effects of a complex background could explain why ΔM_λ increases at larger radii ($R_{cat} > 2'$), as visible in Figure 7. This could also explain why bubbles for which ΔM_λ is below zero ($F_{\lambda,Ap.} < F_{\lambda,Segm.}$) all have a low S/N. Thus, the fact that low S/N bubbles preferentially leads to $\Delta M_\lambda < 0$ seems to suggest that the segmentation is the better choice, when available, for the flux measurements of extended sources.

The good agreement between aperture and segmentation photometry stands out, especially at short wavelengths, with a difference $|\Delta M_\lambda| < 0.1$ for 65%, 68% and 81% of the cases at 12 μm , 22 μm and 70 μm , respectively. The distribution becomes more widely spread at 160 μm as visible in Figures 6 and 7 and as indicated by $\langle \Delta M_\lambda \rangle$ in

Table 3. This is a consequence of a dominant emission from the background that, moving red-ward, increasingly contaminates the flux measurements. At 160 μm , the number of bubbles with $|\Delta M_\lambda| < 0.1$ drops significantly to 19% and at 250 μm to 14%, with average relative difference that could reach $\sim 50\text{--}90\%$.

As showed in Table 2, we found that the active contour segmentation method failed for about 45% of the detected bubbles. The reason of such a fraction of failed segmentation could be attributed to the presence of a possibly complex background, which is expressed by a low S/N of the measurements.

We split the bubbles in *extended* ($R_{cat} > 60''$) and *compact* ($R_{cat} \leq 60''$) sources and showed in Figure 9 the relative distribution of bubbles with a failed segmentation as a function of the S/N. Since no S/N is estimated for non-segmented bubbles, for consistency we used that from aperture photometry instead. As expected extended bubbles

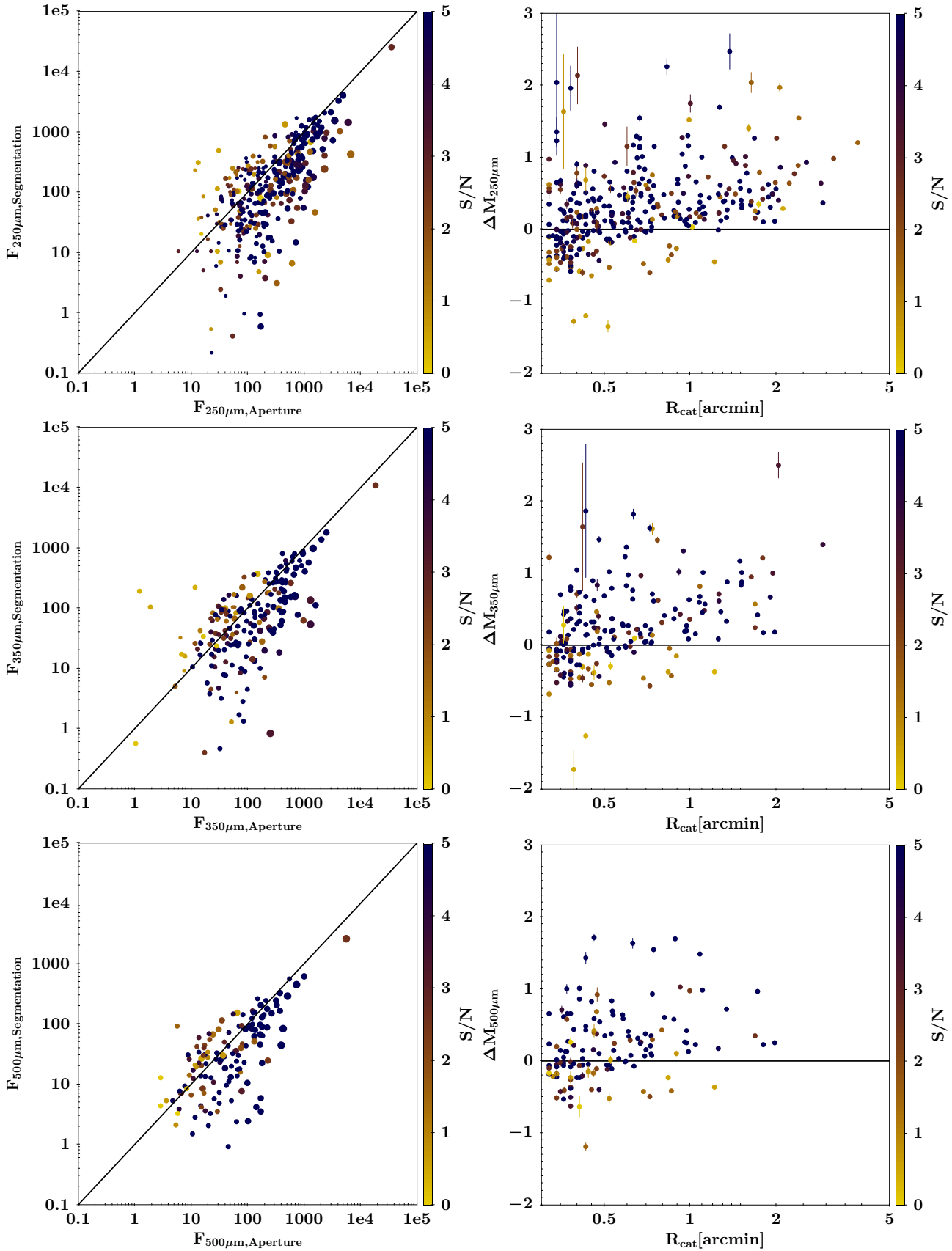


Figure 8. *Left Column:* Comparison of flux estimates using the aperture photometry against the segmentation one. Dots size is proportional to the logarithm of the bubble radius (R_{cat}). *Right Column:* Distribution of flux differences between aperture and segmentation photometric method as function of the angular extension of the bubble. Radii are given in arcminutes. For all the plots, color scales based on the S/N of the relative aperture flux estimation.

Table 3. Average difference between bubbles fluxes measured with aperture and segmentation photometric method. The number of “clipped” bubbles over the total number of bubbles are given, which turn out to be “bright” after the application of both two methods.

Band	$\langle \Delta M_\lambda \rangle$	Clipped/Bright Bubbles
12 μm	0.06 ± 0.11	954/1008
22 μm	0.06 ± 0.07	950/1012
70 μm	0.03 ± 0.05	935/1020
160 μm	0.23 ± 0.37	632/663
250 μm	0.28 ± 0.47	336/346
350 μm	0.25 ± 0.52	203/206
500 μm	0.18 ± 0.47	136/138

with strong contamination or the presence of a structurally complex background affects the boundary found by the algorithm. Indeed, at 70 μm the fraction of extended bubbles with a failed segmentation is equal to 55%, and 92% of them has a S/N lower than 5 (see Figure 9), while such fraction is $\sim 70\%$ if we include segmented bubbles.

For compact bubbles, such effect seems to affect the distribution less, since they are characterized by a lower fraction of unsegmented bubbles with low S/N than the extended bubbles: 40% of compact bubbles have a failed segmentation, and 76% of them are characterized by a S/N < 5 , corresponding to a slightly smaller fraction ($\sim 64\%$) compared to the whole low S/N sample. This confirms that extended bubbles are more affected by the failures of the segmentation method surely because of the background contamination.

Average $\langle \Delta M_\lambda \rangle$ is always positive at all bandpasses and increases moving to longer wavelengths: the relative difference between the two methods obtained from ΔM_λ is less than 15% for 12 μm and 22 μm and goes up to 50–70% at longer wavelengths with a peak at 250 μm ($\sim 93\%$). This effect clearly points to a relevant flux contamination from the background. This is supported also by the steep drop of the number of bright bubbles (see Table 3). In Figure 10, we show the cumulative distributions of segmented compact and extended bubbles at 70 μm and 250 μm as function of the S/N of the flux measurements. The S/N characterizing the bubbles sensibly decreases at longer wavelengths due to a stronger background emission or/and to a weaker source emission: the fraction of extended bubbles with a S/N > 5 goes from 53% at 70 μm down to 21% at 250 μm , while for compact bubbles the fraction changed from 72% to 39% at 70 μm and 250 μm , respectively.

Thus, giving the underestimation of the total emitted flux of the segmentation method with respect to the aperture observed in Fig. 6 and obtained from the analysis of low S/N bubbles, segmentation method demonstrates to be closer to the real flux than the aperture one. Nevertheless, when using it, the fact that the real shape of the bubble contours at $\lambda \neq 70 \mu\text{m}$ could differ from that assumed by using the segmentation masks should be taken into consideration.

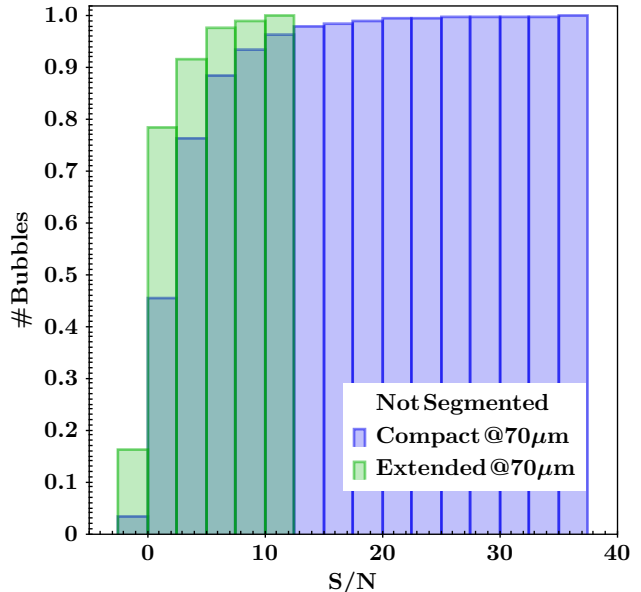


Figure 9. Cumulative distribution of bubbles with failed segmentation at 70 μm as function of the S/N from aperture flux estimation.

7 CONCLUSIONS

This work, born in the wide framework of the VIALACTEA project⁵, has been inspired by the unique opportunity that *Herschel* telescope offers, thanks to its sensitivity and its large wavelength coverage in the far infrared, to derive the physical conditions in Galactic bubbles, whose origins can radically differ being the yield of different stages of star evolution. We took advantage of the availability of the wide image dataset collected from the Hi-GAL survey, flanked it with the *WISE* survey data sampling the emissions at shorter wavelengths, and produced the most extensive catalogue of IR fluxes of extended sources. Thus, in this work, we presented the fluxes of a golden sample of 1814 Galactic bubbles taken from Simpson et al. (2012), acquired at 12 μm , 22 μm , 70 μm , 160 μm , 250 μm , 350 μm and 500 μm bandpasses.

We used two approaches for the flux estimation: a classical aperture photometry and a more innovative method, based on the use of segmentation masks, produced by an image analysis algorithm, called active contour, which defines the boundaries of the bubbles (see Appendix A for a brief explanation of the method). In both methods, we used the bubbles dimension provided by Simpson et al. (2012), to define a circular aperture region centered on the bubble centroid where we estimated the source fluxes and an annular region around it for the local average background level definition. Fluxes obtained with both aperture and segmentation photometry were checked comparing them with those of a more limited sample of H II regions and PNe from A12, obtained with an interactive method. We found a very good agreement, especially with the aperture method results. On the other hand, segmentation photometry seems to work better at short wavelengths but fails over compact objects, for

⁵ <http://vialactea.iaps.inaf.it>

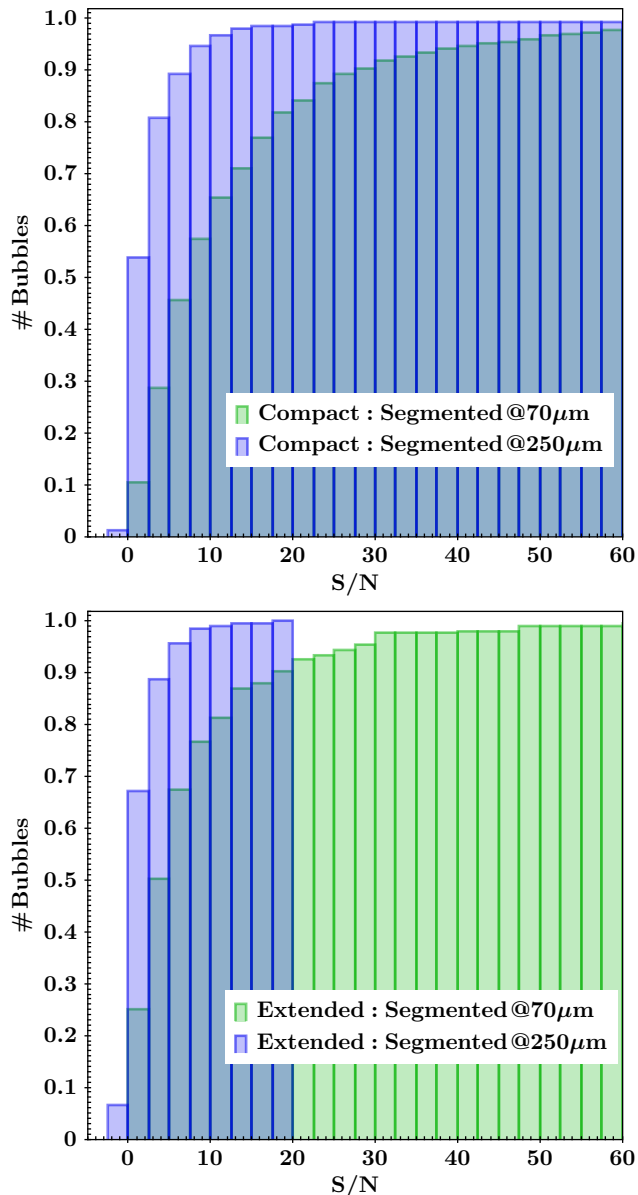


Figure 10. Cumulative distribution of segmented bubbles at $70\ \mu\text{m}$ and $250\ \mu\text{m}$ as function of the S/N of the aperture flux estimation.

which segmentation algorithm shows to have a high failure rate in producing bubble masks.

Finally we compared fluxes of the golden sample bubbles obtained with the two methods, finding a very good agreement especially at the shorter wavelengths (average difference does not exceed 15%). Generally, aperture photometry fluxes turn out to be larger than the segmentation ones, possibly a consequence of a contaminating complex background, whose subtraction can be a tricky task. Indeed such effect gets stronger at long wavelengths ($>160\ \mu\text{m}$) where background dust emission increases.

With this work we offer for the first time a wide catalogue of bubble IR fluxes, produced using fully automated methods. This kind of approach, together with automated algorithms using for instance data mining capabilities for e.g. the source extraction of extended sources or the automated definition

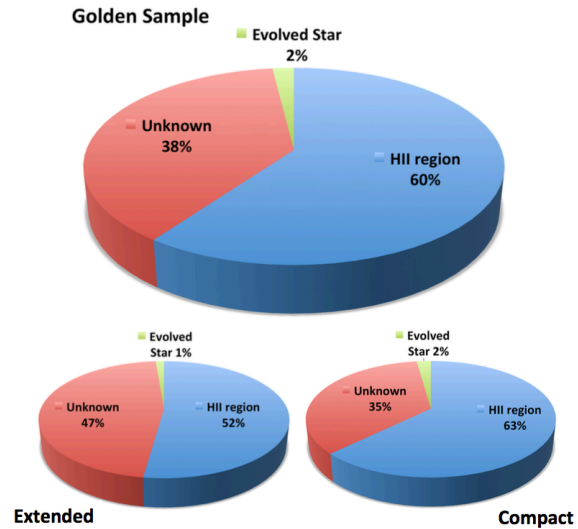


Figure 11. Fraction of classified/unclassified golden sample bubbles from SIMBAD database.

of the source contours (see e.g. Carey et al, in prep; Riggi et al. 2016), is a necessary choice in the astrophysical data analysis considering the new generation instruments (e.g. LSST in the optical, JWST in the IR and SKA at the radio frequencies), which will survey wide sky regions providing a gigantic amount of data.

We checked, querying the SIMBAD astronomical database (Wenger et al. 2000)⁶, if the bubbles in the golden sample have been identified with a specific star evolution event. We considered all the objects in a circular area of radius R_{cat} centered on each bubble centroid coordinates and selected the one at the minimum distance as the literature object associated with the bubble (assuming negligible the probability of false matches coming from perspective coincidences). Finally, we split the objects in *H II regions*, *Evolved Stars* (which includes LBV stars, AGB and post-AGB stars, SNRs, PNe, etc.) and *Unknown*. We noticed that the fraction of bubbles that are classified as *H II regions* is the highest one (60%), against the very low 2% of the evolved stars (see Figure 11). Fractions do not change significantly if we split bubbles in *extended* and *compact*, as done in the previous Section. In any case, a large fraction (38%) remains unclassified. Such finding together with the future perspective of large amount of available data, strengthens the need for an automated method for the bubbles classification, possibly based on their Spectral Energy Distribution and/or on their morphology at different wavelength. This issue exceeds the purpose of this work, but it will be matter of discussion of a forthcoming paper.

⁶ We noticed that *H II regions* identified by Anderson et al. (2014), as well as Anderson et al. (2011) and Paladini et al. (2003), were not included in the SIMBAD database. Thus, we additionally check on such catalogues for our statistics.

ACKNOWLEDGMENTS

The authors acknowledge the anonymous referee for the very useful comments that helped in improving the paper. This work is part of the VIALACTEA Project, a Collaborative Project under Framework Programme 7 of the European Union, funded under Contract # 607380 that is hereby acknowledged. F.B. acknowledges support from the VIALACTEA Project. *Herschel* is an ESA space observatory with science instruments provided by European-led Principal Investigator consortia and with important participation from NASA. PACS has been developed by a consortium of institutes led by MPE (Germany) and including UVIE (Austria); KUL, CSL, IMEC (Belgium); CEA, OAMP (France); MPIA (Germany); IAPS, OAP/OAT, OAA/CAISMI, LENS, SISSA (Italy); IAC (Spain). This development has been supported by the funding agencies BMVIT (Austria), ESA-PRODEX (Belgium), CEA/CNES (France), DLR (Germany), ASI (Italy), and CICYT/MCYT (Spain). SPIRE has been developed by a consortium of institutes led by Cardiff Univ. (UK) and including Univ. Lethbridge (Canada); NAOC (China); CEA, LAM (France); IAPS, Univ. Padua (Italy); IAC (Spain); Stockholm Observatory (Sweden); Imperial College London, RAL, UCL-MSSL, UKATC, Univ. Sussex (UK); Caltech, JPL, NHSC, Univ. Colorado (USA). This development has been supported by national funding agencies: CSA (Canada); NAOC (China); CEA, CNES, CNRS (France); ASI (Italy); MCINN (Spain); Stockholm Observatory (Sweden); STFC (UK); and NASA (USA).

This publication makes use of data products from the Wide-field Infrared Survey Explorer, which is a joint project of the University of California, Los Angeles, and the Jet Propulsion Laboratory/California Institute of Technology, funded by the National Aeronautics and Space Administration. This research has made use of the SIMBAD database, operated at CDS, Strasbourg, France. This research made use of Montage. It is funded by the National Science Foundation under Grant Number ACI-1440620, and was previously funded by the National Aeronautics and Space Administration's Earth Science Technology Office, Computation Technologies Project, under Cooperative Agreement Number NCC5-626 between NASA and the California Institute of Technology.

REFERENCES

- Akram, F., Kim, J. H., Lim, H. U., & Choi, K. N., 2014, Computational and Mathematical Methods in Medicine, 194614
- Anderson L. D., Bania T. M., Balsler D. S., Cunningham V., Wenger T. V., Johnstone B. M., Armentrout W. P., 2014, ApJS, 212, 1
- Anderson L. D., Zavagno A., Barlow M. J., García-Lario P., Noriega-Crespo A., 2012, A&A, 537, 1, [A12]
- Anderson L. D., Bania T. M., Balsler D. S., Rood R. T., 2011, ApJS, 194, 32
- Balog Z., et al., 2014, ExA, 37, 129
- Bendo G. J., et al., 2013, MNRAS, 433, 3062
- Benjamin R. A., et al., 2003, PASP, 115, 953
- Carey S. J., et al., 2009, PASP, 121, 76
- Churchwell E., et al., 2007, ApJ, 670, 428
- Churchwell E., et al., 2006, ApJ, 649, 759
- Deharveng L., et al., 2010, A&A, 523, A6
- Griffin M. J., et al., 2010, A&A, 518, L3
- Hummel R. A., 1977, Image Enhancement by Histogram Transformation. Computer Graphics and Image Processing 6, 184195
- Lankton S., Tannenbaum A., 2009, IEEE Trans. Image Process., vol. 17, no. 11, pp. 20292039.
- Mizuno D. R., et al., 2010, AJ, 139, 1542
- Molinari S., et al., 2016, A&A, 591, A149
- Molinari S., et al., 2010, A&A, 518, L100
- Paladini R., et al., 2012, ApJ, 760, 149
- Paladini R., Burigana C., Davies R. D., Maino D., Bersanelli M., Cappellini B., Platania P., Smoot G., 2003, A&A, 397, 213
- Pilbratt G. L., et al., 2010, A&A, 518, L1
- Poglitsch A., et al., 2010, A&A, 518, L2
- Riggi S., et al., 2016, MNRAS, 460, 1486
- Rogers E., Zack G. W., 1977, J. Histochem. Cytochem., vol. 25, no. 7, pp. 1114
- Simpson R. J., et al., 2012, MNRAS, 424, 2442
- Tielens A. G. G. M., 2008, ARA&A, 46, 289
- Traficante A., et al., 2011, MNRAS, 416, 2932
- Volk K., Kwok S., 2003, IAUS, 209, 303
- Wachter S., Mauerhan J. C., Van Dyk S. D., Hoard D. W., Kafka S., Morris P. W., 2010, AJ, 139, 2330
- Wang, L., He, L., Mishra, A., & Li, C., 2009, Active contours driven by local Gaussian distribution fitting energy. Signal Processing, 89(12), 24352447.
- Wenger M., et al., 2000, A&AS, 143, 9
- Wright E. L., et al., 2010, AJ, 140, 1868-1881
- Xie X., and Mirmehdi M., 2008, IEEE Trans. Pattern Anal. Mach. Intell., vol. 30, no. 4, pp. 632646.
- Yang, Q., & Boukerroui, D., 2012, Ultrasound segmentation using localised active contours with adaptive statistics. IEEE, 10961099.
- Yilmaz, A., Javed, O., & Shah, M. (2006). Object Tracking: A Survey. ACM Computing Surveys, 38(4).

APPENDIX A: THE ACTIVE CONTOURS METHOD FOR SEGMENTATION

Active Contours are a family of popular curve deformation techniques that are often applied within computer vision for the unsupervised segmentation of image objects. Their simple mode of operation has allowed them to be applied to a variety of different problems (Akram et al. 2014; Lankton & Tannenbaum 2009; Yilmaz et al. 2006). They are especially useful in instances where the use of supervised machine learning approaches is implausible. This is because labelled data is expensive to generate and the robustness of these techniques makes them good candidates for situations where there is a lack of expert annotations. However, the drawback of most contouring methods is that they come with the caveat that parameters have to be substantially adjusted before segmentations will meet human expectations. For example, a well-established, and parameter heavy, Active Contour model is the Localised Variant (Lankton & Tannenbaum 2009; Wang et al. 2009; Yang & Boukerroui 2012) which evaluates contour deformation functions within the bounds of predefined kernels. The size of the kernels

largely dictate the end segmentation result and since they have to be defined a priori, its use in real world problems is often limited. Therefore, this paper addresses the above issue with a novel generic adaptive kernel selection scheme that also makes use of the sign of Magnetostatic forces (Xie & Mirmehdi 2008). The use of signed electrostatic information enables textured foreground regions to be delineated from low gradient background areas. However, as astronomy images are composed of complex objects of varying intensity, the segmentation results of Magnetostatic Active Contours cannot be relied upon and more appropriate results are achieved when this technique is aided by local statistical information. The main steps adopted in this paper are reported in the following text, while a more detailed description of the method is given in Carey et al. (2017, in prep.).

A1 Preprocessing

The above approaches work best when the image data under consideration is made more amenable to segmentation. In this work, preprocessing amounted to: adjusting the dynamic range of the original image data by selecting a log transformation coefficient which maximised the correlation between the transformed and the log of the original data's numerical gradients; locally maximising the contrast (defined as the difference in intensity between local pixels) of the transformed data; data smoothing and compression via a discrete wavelet transformation and appropriately initialising the active contour algorithm.

Automatic Log Exponent Selection– Log transformation is a standard tool used in astronomy and results in the compression of the dynamic range of the data. The skewness of the original image, where there are only a few pixels with high intensity values, means that if active contours were applied to this data then it will only fit around very bright objects. Therefore, the difference in intensity between high and low valued pixels needs to be decreased and this is accomplished by Log transformations. When too high exponent values are used in this process, more pixels will reach the maximum transformed intensity value of 255. This will make the boundaries of the bubble features more difficult to locate as is evident from Figure A1 where the definition of the edges of the image object has varying degrees of ambiguity over the range of exponent values used. Notice that when using a value of 10,000, the bright source in the bottom left of the image dominates the local region and the true edge of the object is lost. Therefore, similar problems as using the original image data will persist. The same is true when using exponent values that are too low, where differences in pixel intensity values with respect to the images background are lost. The edges of the transformed data will be weak when definition is lost and so correlating the transformed images gradient with that of the log of the gradient magnitude of the original will mean that an exponent value is selected that preserves as much authentic boundary information as possible.

Local Adaptive Contrast Histogram Equalisation– The selection of an appropriate log transformation preserves as much boundary information as possible but the definition of the objects boundaries and their contrast with respect to the background can still be poor (due to the inherent skewness of the original data). Therefore, a tiling process,

known as Locally Adaptive Contrast Histogram Equalization (LACHE), was used to adjust the local pixel intensity histograms of patches of the original image (Hummel 1977): in this paper a local tile of 40 by 40 pixels was used. The adjustments result in the stretching of the local histograms so that very weak pixels become more apparent. This greatly improves the definition of the bubble features as is apparent when Figure A2 is compared to those present in Figure A1.

Discrete Wavelet Transformation– The localised enhancement of the image features helps in the segmentation process but the large variations introduced by the above process needs to be corrected for. In this instance, this was facilitated by a Discrete Wavelet Transformation (DWT). As LACHE is a local technique, errors in enhancement can happen at the edges of the local tiles this algorithm uses. This can effect where the boundaries of bubble object reside and so this essential smoothing process enables the active contours to better fit the features of interest. DWT not only smooths out the data but also reduces its size.

Initialisation– The starting position of the active contour, from which it will grow, also has a large impact on the end segmentation result. In this papers approach, the incorporation of Magnetostatic forces relieved this difficulty to an extent, but the contours still needed to be started fairly close to object of interest. For example, every pixel in an image will have gradient and these will not necessarily correspond to image objects of interest. Therefore, the simple use of thresholding to provide active contour intialisation points will mean that contours could grow around undesired structures within the data. To avoid this, the triangle thresholding algorithm (Rogers & Zack 1977) was used with the log of the gradient magnitude of the original image data. Its mode of operation is demonstrated in Figure A3. In this technique, a histogram is formed from the log gradient magnitude image. Its maximum peak, the first and last non empty histogram bins, are found so that two triangles can be formed between its two extrema and the largest concavity (the largest distance) found for each triangle allows an objective threshold to be found for automatic active contour initialisation. Since two thresholds are found, the highest is selected for this segmentation pipeline assuming that celestial objects are usually brighter than their background, as usually observed.

A2 Adaptive Kernel Selection

Once the data was made more amenable to segmentation, active contours can be used for segmentation. The approach taken in this paper relied upon the use of gradient and local statistical information. Gradient information was incorporated via Magnetostatic forces and local statistical information was acquired by the use of an adaptive kernel selection scheme. In traditional approaches, the size of the local area used in the collection of image statistics is predetermined but this is unlikely to reflect the changing content of an image over which the contour evolves. To reflect this changing texture, an initial kernel size, set to be 20 by 20 pixels in this paper, is used to compute the local parametric Bhattacharyya distance between the inside and outside regions of an evolving contour which is defined as:

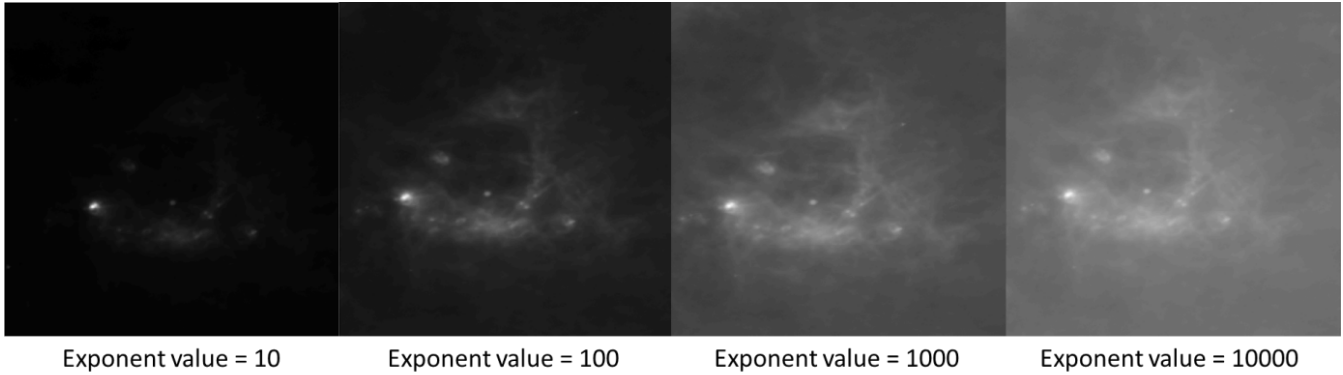


Figure A1. The result of using a range of different exponent values. The gradient magnitude of these are correlated against those of the log of the magnitude of the original data so that an appropriate exponent values can be found.

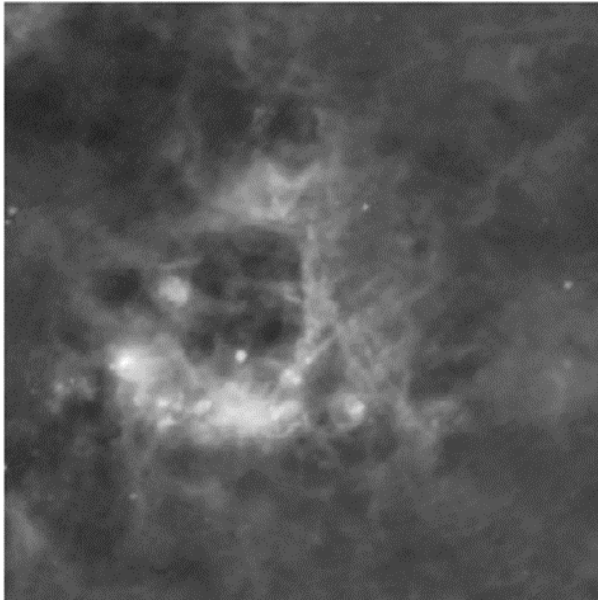


Figure A2. The result of using the 1000 exponent transformed image of Figure A1 with Localised Contrast Enhancement with a tile size of 40 by 40 pixels.

$$BD = \exp\left(-\frac{1}{4}\ln\left(\frac{1}{4}\left(\frac{\sigma_{in}^2}{\sigma_{out}^2} + \frac{\sigma_{out}^2}{\sigma_{in}^2} + 2\right)\right)\right) + \frac{1}{4}\left(\frac{(\mu_{in} - \mu_{out})^2}{\sigma_{in}^2 + \sigma_{out}^2}\right) \quad (A1)$$

where μ and σ are the respective mean and standard deviations of the intensities on the inside and outside of a local region around the evolving contour. This gives a normalised measure of how similar the inside and outside regions of the evolving curve are, allowing large kernels to be selected for regions of homogeneity and small sizes for areas of texture. The weighting of this with a user defined parameter, τ (set to be 0.5 throughout), allowed kernel sizes to be selected in a single pass approach by multiplying Equation A1 with a maximum desired kernel size. Once appropriate kernel sizes have been selected, any localised regional evolution function

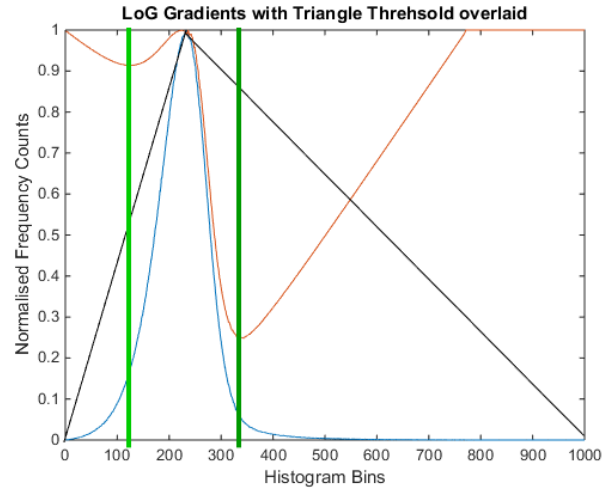


Figure A3. A histogram of the original images Log gradients. The blue line is the histogram, the black lines are the triangles formed by the triangle thresholding, the red lines are the distances of the histograms bin counts away from their nearest triangle hypotenuse and the green line are the selected threshold points. Please note that the red lines contained in the chart do not relate to the y axis. Depending on the distance calculation used - the calculated "distance" can either be negative or positive. In this case, the negative output was used so the largest negative value was found for the selected thresholds.

can be used. In this instance, the following function was used to guide contours towards salient objects:

$$F(x) = \frac{(I(x) - \mu_{in})^2}{2\sigma_{in}^2} - \frac{(I(x) - \mu_{out})^2}{2\sigma_{out}^2} + \log\left(\frac{\sigma_{out}}{\sigma_{in}}\right) \quad (A2)$$

where F is the active contour energy, I is the image of interest, x is a point along the evolving contour and the rest of the nomenclature is the same as Eq. A1.

Experiments have suggested that the choice of the weighting parameter, as well as the quality of the underlying data and the initial kernel size used to probe texture has little effect on the end segmentation result, e.g. Figure A4. We calculated the Dice values, which are a measure of how well automatically generated segmentations overlap with ground truths. For the results within Figure A4, Dice values vary

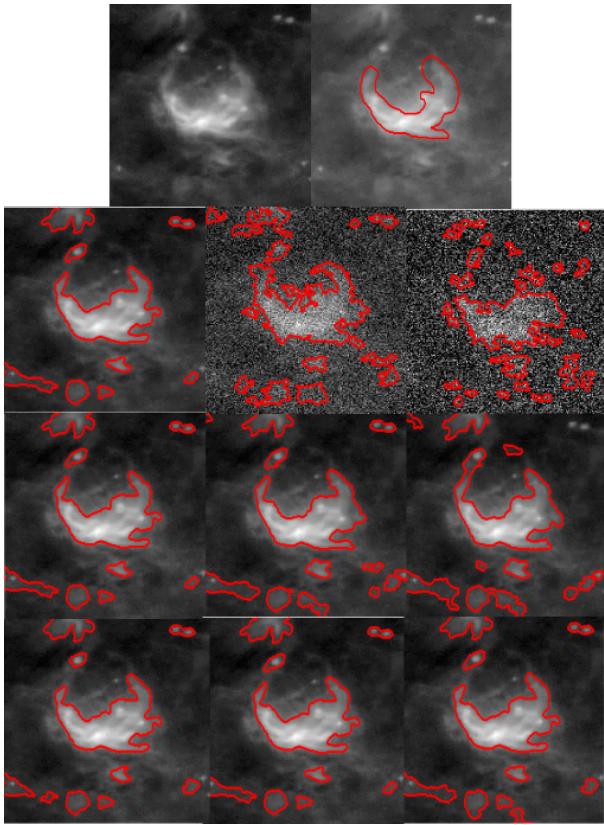


Figure A4. The effect of noise and parameters on segmentation quality. Top row) The original data and an astronomer ground truth in red. Second row) The effect of Gaussian noise of zero mean and 0, 0.01 and 0.03 variance on the segmentation. Third row) The effect of different τ values (0.5, 1 and 2) with a fixed initial kernel size. Fourth row) The effect of different initial kernel sizes (10 by 10 pixels, 20 by 20 pixels and 40 by 40 pixels).

within a fairly decent range of 0.55 (in the extreme noise case) to 0.84.

A3 Magnetostatic Forces

The sole reliance on either localised or Magnetostatic forces to bring about acceptable segmentations is limiting and this is evident from Figure A5. In this figure, a comparison is made against the use of just Magnetostatic information for segmentation against its combination with local image statistics. It can be seen that this complementary methodology can aid the image segmentation process. It is also preferable to just using local information as the whole process would then be reliant upon the statistical approximation being made.

Magnetostatic forces are derived via a magnetic density flux coefficient matrix, \mathbf{B} , which is given by:

$$e1 = g \cdot (-\nabla y \otimes) \frac{1}{r^2} \quad ; \quad e2 = g \cdot \nabla x \otimes \frac{1}{r^2}$$

$$\mathbf{B} = \nabla e2 - \nabla e1 \quad (\text{A3})$$

Where \otimes is the convolution operation performed in the frequency domain, g is the gradient magnitude of the image and r^2 is a centred Euclidean distance matrix padded to

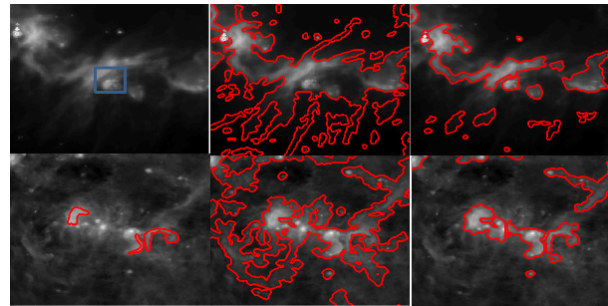


Figure A5. The improved results achieved when adaptive local active contours are used with Magnetostatic forces. The first column is the original data with examples of objects of interest highlighted by blue boxes/red outlines. The middle column is the Magnetostatic forces by themselves and the last column is the result of the adaptive localised contour.

the maximum length of an image of interest for frequency filtering. Magnetostatic forces operate by creating a signed map of where regions of gradient reside in an image and the simple thresholding of this at zero, or another user defined constant, produces a mask which can constrain the growth of the contour around areas of high gradient. This negates the use of background areas in the statistical analysis step of the segmentation.

The refinement of the segmentation with Magnetostatic field diffusion and local image statistics has enabled an image segmentation pipeline that requires little human intervention. Intervention in this paper, took the form of experimenting with different active contour energies and testing different kernel selection schemes. There is unlikely to ever be one active contour method that would be suitable for all astronomy data and an investigation of this sort should always be conducted before any attempt at the use of active contours is made. However, currently the segmentation just provides outlines of astronomical objects and makes no discrimination between the features it finds. Therefore, in the future, approaches will be developed that will allow machine learning techniques to be utilised in the identification of objects of interest (bubbles for example).

APPENDIX B: PHOTOMETRY TABLES

Table B1. Golden Sample Aperture Photometry at 12 μm and 22 μm .

Bubble ID	Long ^a (deg)	Lat ^a (deg)	R_{cat} ^b (arcsec)	12 μm			22 μm		
				Flux (Jy)	err (Jy)	S/N	Flux (Jy)	err (Jy)	S/N
MWP1G358760-007700S	358.76	-0.77	21.6	0.72	0.01	3.1	2.01	0.06	4.6
MWP1G358770+001090	358.77	0.109	20.2	0.25	0.01	5.3	1.00	0.06	4.4
MWP1G358840-007400S	358.84	-0.74	27.0	2.27	0.01	5.3	6.66	0.07	22.1
MWP1G358881+000576	358.881	0.058	40.0	18.02	0.02	33.5	52.88	0.13	27.2
MWP1G358890+000800S	358.89	0.08	20.4	1.15	0.01	8.5	2.81	0.06	9.2
MWP1G358950-000200S	358.95	-0.02	25.2	1.31	0.01	4.1	3.44	0.10	1.7
MWP1G359275-000403	359.275	-0.04	23.5	1.99	0.03	1.9	12.69	0.13	2.8
MWP1G359282-008955	359.282	-0.895	83.0	7.78	0.06	0.4	7.33	0.21	0.3
MWP1G359300+002883	359.3	0.288	195.7	55.49	0.14	0.3	162.05	0.56	0.3
MWP1G359350-004141	359.35	-0.414	49.5	2.68	0.03	1.9	34.60	0.14	7.3
MWP1G359411+000363	359.411	0.036	42.6	10.31	0.07	1.9	60.63	0.19	5.4
MWP1G359420+000200S	359.42	0.02	19.2	1.76	0.03	0.4	12.47	0.15	1.4
MWP1G359450-000200S	359.45	-0.02	24.0	0.23	0.02	0.2	7.63	0.12	1.5
MWP1G359514+002727	359.514	0.273	166.0	16.87	0.12	0.2	198.83	0.51	1.8
MWP1G359569-004772	359.569	-0.477	199.0	–	–	–	–	–	–
MWP1G359740-005900S	359.74	-0.59	22.8	1.62	0.01	6.8	7.16	0.06	34.8
...									

^a Bubble Galactic Coordinates given by Simpson et al. (2012).

^b R_{cat} is taken from Simpson et al. (2012) catalogue and corresponds to the effective radius for the small bubbles or to half the outer diameter in case of large ones.

Table B2. Golden Sample Segmentation Photometry at 12 μm and 22 μm .

Bubble ID	Long ^a (deg)	Lat ^a (deg)	R_{cat} ^b (arcsec)	12 μm			22 μm		
				Flux (Jy)	err (Jy)	S/N	Flux (Jy)	err (Jy)	S/N
MWP1G358760-007700S	358.76	-0.77	21.6	0.85	0.01	4.0	2.25	0.06	5.7
MWP1G358770+001090	358.77	0.109	20.2	–	–	–	–	–	–
MWP1G358840-007400S	358.84	-0.74	27.0	2.41	0.01	6.3	6.62	0.06	21.5
MWP1G358881+000576	358.881	0.058	40.0	17.10	0.02	23.9	49.11	0.10	23.0
MWP1G358890+000800S	358.89	0.08	20.4	0.91	0.01	4.4	1.80	0.04	4.0
MWP1G358950-000200S	358.95	-0.02	25.2	1.27	0.01	3.2	4.60	0.07	3.0
MWP1G359275-000403	359.275	-0.04	23.5	–	–	–	–	–	–
MWP1G359282-008955	359.282	-0.895	83.0	–	–	–	–	–	–
MWP1G359300+002883	359.3	0.288	195.7	–	–	–	–	–	–
MWP1G359350-004141	359.35	-0.414	49.5	2.34	0.01	1.5	7.57	0.06	3.3
MWP1G359411+000363	359.411	0.036	42.6	–	–	–	–	–	–
MWP1G359420+000200S	359.42	0.02	19.2	–	–	–	–	–	–
MWP1G359450-000200S	359.45	-0.02	24.0	–	–	–	–	–	–
MWP1G359514+002727	359.514	0.273	166.0	–	–	–	–	–	–
MWP1G359569-004772	359.569	-0.477	199.0	–	–	–	–	–	–
MWP1G359740-005900S	359.74	-0.59	22.8	1.48	0.01	4.3	6.78	0.05	23.9
...									

^a Bubble Galactic Coordinates given by Simpson et al. (2012).

^b R_{cat} is taken from Simpson et al. (2012) catalogue and corresponds to the effective radius for the small bubbles or to half the outer diameter in case of large ones.

Table B3. Golden Sample Aperture Photometry at 70 μm , 160 μm , 250 μm , 350 μm and 500 μm .

Bubble ID	Long ^a (deg)	Lat ^a (deg)	R_{cat} ^b (arcsec)	70 μm			160 μm			250 μm			350 μm			500 μm		
				Flux (Jy)	err (Jy)	S/N	Flux (Jy)	err (Jy)	S/N	Flux (Jy)	err (Jy)	S/N	Flux (Jy)	err (Jy)	S/N	Flux (Jy)	err (Jy)	S/N
MWP1G358760-007700S	358.76	-0.77	21.6	47.20	0.68	6.3	128.25	2.22	9.8	89.05	1.74	7.3	49.06	1.13	7.7	18.37	0.62	7.1
MWP1G358770+001090	358.77	0.109	20.2	23.39	1.15	3.5	31.23	6.15	0.7	17.52	4.58	0.5	4.65	2.57	0.6	4.03	1.16	0.7
MWP1G358840-007400S	358.84	-0.74	27.0	166.08	0.99	20.5	289.98	3.48	11.1	179.74	2.82	8.7	87.14	1.86	8.1	31.63	0.96	9.0
MWP1G358881+000576	358.881	0.058	40.0	1103.74	6.95	11.4	789.43	12.56	5.9	372.57	7.56	4.5	170.20	4.10	4.5	59.86	1.91	4.5
MWP1G358890+000800S	358.89	0.08	20.4	98.44	1.88	6.7	148.42	6.62	3.2	84.45	5.64	2.1	29.93	4.48	1.4	13.25	2.67	0.9
MWP1G358950-000200S	358.95	-0.02	25.2	57.45	5.42	0.8	44.45	7.86	1.3	41.75	4.26	2.3	22.82	2.45	2.8	13.90	1.23	3.7
MWP1G359275-000403	359.275	-0.04	23.5	243.59	5.40	3.2	155.56	14.64	0.6	59.48	11.92	0.4	29.32	7.17	0.4	16.79	3.54	0.4
MWP1G359282-008955	359.282	-0.895	83.0	181.10	4.89	0.1	561.47	15.14	0.3	292.88	9.32	0.3	116.16	4.97	0.3	40.35	2.21	0.4
MWP1G359300+002883	359.3	0.288	195.7	2875.17	22.17	0.2	7833.53	51.46	0.9	4420.15	30.40	1.4	1995.04	16.34	1.6	660.95	7.46	1.6
MWP1G359350-004141	359.35	-0.414	49.5	12.27	3.31	0.5	70.59	8.79	0.9	84.00	5.12	1.4	52.52	2.73	2.0	21.17	1.32	2.3
MWP1G359411+000363	359.411	0.036	42.6	1262.36	9.62	3.6	973.32	15.11	2.0	256.28	9.06	0.3	59.42	5.07	-0.6	11.02	2.50	-0.7
MWP1G359420+000200S	359.42	0.02	19.2	411.34	6.92	2.8	345.95	13.36	2.2	88.14	10.27	0.9	41.18	5.30	1.1	20.67	2.27	1.4
MWP1G359450-000200S	359.45	-0.02	24.0	***	***	***	-267.39	15.42	-1.4	***	***	***	***	***	***	***	***	***
MWP1G359514+002727	359.514	0.273	166.0	3960.82	12.21	1.9	3574.36	46.98	0.4	564.90	36.44	-0.1	116.42	20.75	-0.2	45.81	9.36	-0.2
MWP1G359569-004772	359.569	-0.477	199.0	8392.94	18.38	1.6	8238.16	72.53	0.4	1229.62	55.34	-0.0	242.08	30.33	-0.1	42.60	13.86	-0.2
MWP1G359740-005900S	359.74	-0.59	22.8	111.24	0.97	9.6	104.36	1.88	10.7	-	-	-	-	-	-	-	-	-
...																		

^a Bubble Galactic Coordinates given by Simpson et al. (2012).

^b R_{cat} is taken from Simpson et al. (2012) catalogue and corresponds to the effective radius for the small bubbles or to half the outer diameter in case of large ones.

Table B4. Golden Sample Segmentation Photometry at 70 μm , 160 μm , 250 μm , 350 μm and 500 μm .

Bubble ID	Long ^a (deg)	Lat ^a (deg)	R_{cat} ^b (arcsec)	70 μm			160 μm			250 μm			350 μm			500 μm		F _{BU} /R ₀ [Eq. 4]	
				Flux (Jy)	err (Jy)	S/N	Flux (Jy)	err (Jy)	S/N	Flux (Jy)	err (Jy)	S/N	Flux (Jy)	err (Jy)	S/N	Flux (Jy)	err (Jy)		
MWP1G358760-007700S	358.76	-0.77	21.6	47.15	0.22	10.0	235.62	3.00	1.9	158.04	1.91	2.0	72.29	0.86	2.3	21.47	0.32	-	
MWP1G358770+001090	358.77	0.109	20.2	-	-	-	-	-	-	-	-	-	-	-	-	-	-	-	
MWP1G358840-007400S	358.84	-0.74	27.0	165.75	0.41	19.8	280.10	2.80	3.3	107.62	0.63	9.3	40.84	0.32	9.2	4.80	0.12	-	
MWP1G358881+000576	358.881	0.058	40.0	1102.47	2.34	12.1	527.76	8.96	2.1	***	***	***	***	***	***	***	***	-	
MWP1G358890+000800S	358.89	0.08	20.4	85.73	0.63	5.6	***	***	***	***	***	***	***	***	***	***	***	-	
MWP1G358950-000200S	358.95	-0.02	25.2	131.68	1.00	4.1	452.10	9.99	1.4	168.01	5.60	1.5	67.34	2.39	1.5	22.26	0.81	1.6	
MWP1G359275-000403	359.275	-0.04	23.5	-	-	-	-	-	-	-	-	-	-	-	-	-	-	-	
MWP1G359282-008955	359.282	-0.895	83.0	-	-	-	-	-	-	-	-	-	-	-	-	-	-	-	
MWP1G359300+002883	359.3	0.288	195.7	-	-	-	-	-	-	-	-	-	-	-	-	-	-	-	
MWP1G359350-004141	359.35	-0.414	49.5	59.75	0.53	0.3	***	***	***	***	***	***	***	***	***	***	***	***	
MWP1G359411+000363	359.411	0.036	42.6	-	-	-	-	-	-	-	-	-	-	-	-	-	-	-	
MWP1G359420+000200S	359.42	0.02	19.2	-	-	-	-	-	-	-	-	-	-	-	-	-	-	-	
MWP1G359450-000200S	359.45	-0.02	24.0	-	-	-	-	-	-	-	-	-	-	-	-	-	-	-	
MWP1G359514+002727	359.514	0.273	166.0	-	-	-	-	-	-	-	-	-	-	-	-	-	-	-	
MWP1G359569-004772	359.569	-0.477	199.0	-	-	-	-	-	-	-	-	-	-	-	-	-	-	-	
MWP1G359740-005900S	359.74	-0.59	22.8	109.41	0.37	11.5	14.05	0.52	8.8	-	-	-	-	-	-	-	-	-	
...																			

^a Bubble Galactic Coordinates given by Simpson et al. (2012).^b R_{cat} is taken from Simpson et al. (2012) catalogue and corresponds to the effective radius for the small bubbles or to half the outer diameter in case of large ones.